submitted to *Geophys. J. Int.*

3D wave propagation and earthquake dynamic rupture simulations in complex poroelastic media

Sebastian Wolf[1], Alice-Agnes Gabriel[2,3⋆], Martin Galis[4,5], Peter Moczo[4,5],
David Gregor[6], Michael Bader[1]

[1] Technical University of Munich

[2] Scripps Institution of Oceanography, University of California San Diego

[3] Ludwig-Maximilians-Universität München

[4] Comenius University in Bratislava

[5] Slovak Academy of Sciences

[6] Université Grenoble Alpes

SUMMARY

Numerical simulations of earthquakes and seismic wave propagation require accurate material models of the solid Earth. In contrast to purely elastic rheology, poroelasticity accounts for pore fluid pressure and fluid flow in porous media. Poroelastic effects can alter both the seismic wave field and the dynamic rupture characteristics of earthquakes. For example, the presence of fluids may affect cascading multi-fault ruptures, potentially leading to larger-than-expected earthquakes. However, incorporating poroelastic coupling into the elastodynamic wave equations increases the computational complexity of numerical simulations compared to elastic or viscoelastic material models, as the underlying partial differential equations become stiff.

In this study, we use a Discontinuous Galerkin solver with Arbitrary High-Order DERivative time stepping (ADER-DG) of the poroelastic wave equations implemented in the open-source software SeisSol to simulate 3D complex seismic wave propagation and 3D dynamic rupture in poroelastic media. We verify our approach for double-couple point sources using independent methods including a semi-analytical solution and a finite-difference scheme and a homogeneous full-space and a poroelastic layer-over-half-space model, respectively. In a realistic carbon capture and storage (CCS) reservoir scenario at the Sleipner site in the Utsira Formation, Norway, we model 3D wave propagation through poroelastic sandstone layers separated by impermeable shale. Our results show a sudden change in the pressure field across material interfaces, which manifests as a discontinuity when viewed at the length scale of the dominant wavelengths of S- or fast P-waves. Accurately resolving the resulting steep pressure gradient dramatically increases the computational demands, requiring high-resolution modeling. We show that the Gassmann elastic equivalent model yields almost identical results to the fully poroelastic model when focusing solely on solid particle velocities.

We extend this approach using suitable numerical fluxes to 3D dynamic rupture simulations in complex fault systems, presenting the first 3D scenarios that combine poroelastic media with geometrically complex, multi-fault rupture dynamics and tetrahedral meshes. Our findings reveal that, in contrast to modeling wave propagation only, poroelastic materials significantly alter rupture characteristics compared to using elastic equivalent media since the elastic equivalent fails to capture the evolution of pore pressure. Particularly in fault branching scenarios, the Biot coefficient plays a key role in either promoting or inhibiting fault activation. In some cases, ruptures are diverted to secondary faults, while in others, poroelastic effects induce rupture arrest. In a fault zone dynamic rupture model, we find poroelasticity aiding pulse-like rupture. A healing front is induced by the reduced pore pressure due to reflected waves from the boundaries of the poroelastic damage zone.

Our results highlight that poroelastic effects are important for realistic simulations of seismic waves and earthquake rupture dynamics. In particular, our poroelastic simulations may offer new insights on the complexity of multi-fault rupture dynamics, fault-to-fault interaction and seismic wave propagation in realistic models of the Earth's subsurface.

Key words: Computational seismology, Earthquake dynamics, Friction, Permeability and porosity, Wave propagation, Wave scattering and diffraction

1 INTRODUCTION

Poroelasticity integrates concepts from elasticity, fluid dynamics, and geomechanics and enables the coupling of fluid pressure and deformation in porous media, which is important for applications ranging from seismic exploration to monitoring of geological reservoirs and earthquake physics (e.g., Carcione et al. 2010). Poroelastic effects are modulated by the porosity, permeability, and fluid saturation of rocks and can affect the seismic wave field. In addition, the interaction between fluid flow and earthquake fault slip can affect dynamic rupture characteristics in earthquake simulations. Despite remarkable efforts in the laboratory and field (e.g., Plona 1980; Berryman 1980; Carcione 2015), observing poroelastic effects remains a challenge, motivating numerical simulations to accurately represent the interaction between fluid flow and solid deformation in heterogeneous geological settings.

However, to capture these interactions at realistic scales and resolution, numerical simulations require large computational resources. For example, during a reflection and/or transition of seismic waves at/through material interfaces and/or at the free surface in poroelastic materials, a slow diffusive P-wave is generated, which has a small wavelength compared to the fast P-wave and S-wave, and attenuates quickly with distance from its origin (Dutta & Odé 1983). To accurately model the slow P-wave at an interface or free surface, a fine resolution is required to resolve the relative fluid velocities (Wolf et al. 2022).

Poroelastic media can be described by Biot's equations (Biot 1956a,b,c, 1962), and poroelastic effects have been considered in numerical simulations of seismic wave propagation for more than three decades (e.g., Zhu & McMechan 1991; Masson et al. 2006; De Barros et al. 2010; Morency et al. 2011; Moczo et al. 2019; Gregor et al. 2021, 2022). Earthquake dynamic rupture simulations (Harris et al. 2011, 2018; Ramos et al. 2022) account for the non-linear coupling of seismic wave propagation and frictional failure along faults and are a mature tool to advance the understanding of earthquake physics and physics-based seismic hazard assessment (e.g. Oglesby et al. 1998; Harris et al. 2021; Gabriel et al. 2023). While a variety of numerical implementations exist (e.g. Virieux & Madariaga 1982; Cruz-Atienza & Virieux 2004; Kaneko et al. 2008; Barall 2009; Pelties et al. 2012b;

⋆ algabriel@ucsd.edu

Duru & Dunham 2016; Okubo et al. 2020; Gabriel 2021; Hayek et al. 2023), dynamic simulations of earthquake rupture typically assume simplified (elastic, viscoelastic, or visco-elasto-plastic) off-fault material rheologies (e.g. Uphoff et al. 2017; Taufiqurrahman et al. 2022).

New opportunities to address these challenges have emerged with recent advances in high-performance computing (HPC) and the development of advanced numerical methods. It is now possible to simulate earthquake rupture scenarios in poroelastic materials: for example, Pampillón et al. (2018, 2023) and Li & Zhang (2023) highlight pore pressure effects additionally weakening a fault and thus facilitating the transition to supershear rupture. Recently, Wolf et al. (2022) developed an efficient high-order accurate ADER-DG (Arbitrary high-order DERivative Discontinuous Galerkin) scheme for the simulation of seismic waves in 3D poroelastic media, extending the approach introduced by de la Puente (2008). The work presented here extends the approach of Wolf et al. (2022) to double-couple moment tensor point sources, complex 3D geological models, and dynamic rupture simulations accounting for fault branching and fault zone effects.

The remainder of this paper is organized as follows. In section 2.1, we review the theoretical frameworks underlying the poroelastic elastodynamic wave equations and dynamic rupture models. In section 2.2, we briefly summarize the discontinuous Galerkin approach to discretize the poroelastic wave equation. We study poroelastic effects for a moment tensor point source in section 3.1, focusing on the behaviour of pore pressure at material interfaces. We verify the correct implementation of double couple point sources in a homogeneous full-space and in a layer-over-half-space model in comparison to semi-analytical and finite-difference results, respectively. Then, we model the seismic wave field in a realistic carbon capture and storage (CCS) reservoir. In section 3.2, we investigate the effects of poroelasticity on 3D earthquake dynamics for a branching fault model and a fault embedded in a fault damage zone. We discuss our findings, implications, and future research directions that our work motivates in section 4.

2 METHODS

2.1 Statement of the problem

In the following, we briefly summarize the equations governing elastodynamic wave propagation in poroelastic media. Furthermore, we summarize the dynamic rupture source mechanism, which couples seismic wave propagation and frictional failure along pre-defined faults.

A poroelastic medium consists of an elastic matrix, which represents a solid material. The pore space within this matrix is saturated with a fluid. We follow Biot's model that describes the interaction of the matrix and fluid by considering a homogenized material (Biot 1956a,b,c, 1962). As principal quantities, we define the total stress of the combined material σ_{ij}, the solid particle velocities of the matrix u, v, w, the fluid pressure p and the relative fluid velocities u_f, v_f, w_f. We then solve the poroelastic wave equation in the first-order form:

$$\frac{\partial Q_p}{\partial t} + A_{pq}\frac{\partial Q_q}{\partial x} + B_{bp}\frac{\partial Q_q}{\partial y} + C_{pq}\frac{\partial Q_q}{\partial z} = E_{pq}Q_q\,. \tag{1}$$

The vector $Q = (\sigma_{xx}, \sigma_{yy}, \sigma_{zz}, \sigma_{xy}, \sigma_{yz}, \sigma_{xz}, u, v, w, p, u_f, v_f, w_f)$ comprises all unknowns. The values of the flux matrices $A, B, C \in \mathbb{R}^{13\times13}$ and the source matrix $E \in \mathbb{R}^{13\times13}$ are detailed in Appendix A.

The poroelastic material is described by a total of ten different material parameters. The solid matrix is characterized by its density ρ_S and the bulk modulus of the solid material K_S. The drained matrix behaves like an elastic body, i.e., its response to deformation is described by the two Lamé parameters λ_M and μ_M. The matrix and the geometry of the pore space are characterized by the porosity ϕ, the permeability κ, and the tortuosity T. The fluid, which fills the pores, is defined by its bulk modulus K_F, the density ρ_F, and its viscosity ν. A detailed overview of the different parameters and their physical interpretation is given in Carcione (2001); de la Puente (2008) and Figures 2 and 3 in Gregor et al. (2022) illustrate all material parameters. In Appendix A, these parameters occur in the detailed PDE system, Equation (1).

During an earthquake, accumulated stresses are suddenly released in the form of slip along a fault. In a dynamic rupture model, the slip evolution along the fault is not prescribed but develops spontaneously. These simulations require initial conditions – the distribution of initial stresses and the parameters of the frictional constitutive law, which can vary across the fault – in solving the equation of motion together with a frictional, internal boundary condition (Harris et al. 2018; Ramos et al. 2022). Earthquake dynamic rupture models are physically self-consistent. However, they are also computationally expensive (Uphoff et al. 2017). They are useful for studying the physics of earthquakes and seismic ground motions, for example, to study topography effects and the influence of the subsurface velocity model on ground motions Ely et al. (2010), to investigate the potential role of seamounts during the 2011 Mw 9.0 Tohoku, Japan earthquake (Duan 2012), to constrain dynamically plausible rupture propagation along a complex system of faults as during the 2016 Mw 7.8 Kaikoura, New Zealand earthquake (Ulrich et al. 2019), or to study unexpected ruptures across multiple fault segments during the 2023 Mw 7.8 and 7.7 Kahramanmaras, Turkey earthquake doublet (Gabriel et al. 2023).

In our framework, we consider the following fault friction model. The stress field σ along the fault can be decomposed into the normal stress component σ_n and the fault-parallel traction $\vec{\sigma}_t$. The fault strength is computed as $\tau = \mu_f \cdot \sigma_n$, where μ_f is a dimensionless friction coefficient. If the traction is smaller than the fault strength ($\|\vec{\sigma}_t\| < \tau$), the fault remains locked. If the traction exceeds the fault strength, the fault starts to slide. We adopt the convention that the slip rate vector $\vec{s}$ (i.e., the discontinuity in particle velocity across the fault) is parallel to the fault traction: $\vec{s}\tau = \vec{\sigma}_t\|\vec{s}\|$. The effective friction coefficient μ_f is not constant but can vary in time according to the adopted friction law.

In this study, we consider a linear slip-weakening friction law (Andrews 1976). With increasing slip path length φ, the friction coefficient drops linearly from the static value μ_s to the dynamic value μ_d. Co-seismic weakening occurs over the critical slip distance D_c:

$$\begin{aligned} \mu_f(t) &= \max\left(\mu_s - (\mu_s - \mu_d)\cdot\varphi(t)/D_c, \mu_d\right)\,, \\ \varphi(t) &= \int_0^t \|\vec{s}(\xi)\|\mathrm{d}\xi\,. \end{aligned} \tag{2}$$

2.2 Numerical discretisation

Equation (1) is numerically solved using the ADER-DG implementation presented in (Wolf et al. 2022). We discretise the computational domain Ω into a set of non-overlapping and conforming tetrahedral grid cells $\mathcal{E}_i$. Following a Discontinuous Galerkin approach, in each cell, the unknowns $Q_p(t,x,y,z)$ are expanded using a set of polynomials $Q_p(t,x) = \widehat{Q}_{pl}(t)\Psi_l(x,y,z)$, without requesting continuity across elements. The (solely space-dependent) polynomials Ψ_l are defined locally in each cell. The $\widehat{Q}_{pl}$ denote the time-dependent degrees of freedom. We formulate the finite-element-typical weak form, i.e., multiply equation (1) with a test function, and integrate by parts to obtain

$$\begin{aligned} &\frac{\partial\widehat{Q}_{pl}}{\partial t}\int_{\mathcal{E}_i}\Psi_l\Psi_k dV \\ &\qquad - A_{pq}\widehat{Q}_{ql}\int_T \Psi_l\frac{\partial\Psi_k}{\partial x}dV - B_{pq}\widehat{Q}_{ql}\int_T \Psi_l\frac{\partial\Psi_k}{\partial y}dV - C_{pq}\widehat{Q}_{ql}\int_T \Psi_l\frac{\partial\Psi_k}{\partial z}dV \\ &\qquad\qquad + \int_{\partial\mathcal{E}_i} F^*(Q)\Psi_k dS = \widehat{Q}_{ql}\int_{\mathcal{E}_i} E_{pq}\Psi_l\Psi_k dV\,. \end{aligned} \tag{3}$$

In the surface-integral over $\partial\mathcal{E}_i$, the term F^* then denotes the flux of quantities across the cell boundaries. A suitable numerical flux $F(Q^-,Q^+)$, which takes the discontinuity between the solution on the interior Q^- and the solution on the neighbouring element Q^+ into account, is crucial for the convergence of the scheme (LeVeque 2002; Hesthaven & Warburton 2008). The purpose of the numerical flux is to approximate the flow of quantities across the interface. We use the upwind-type Godunov flux (e.g. LeVeque 2002) because it is relatively easy to compute and has favourable approximation properties. The Godunov flux solves the Riemann problem, with the quantities Q^+ and Q^- on both sides of the interface as the initial condition, to first compute the state Q^* at the interface and then the resulting flux: $F(Q^-,Q^+) = \tilde{A}_{pq}Q^*_q$. Here, $\tilde{A} = n_1A + n_2B + n_3C$ is the matrix describing the flux in the direction of the outward pointing normal $\vec{n}$.

The basis functions Ψ are defined by a set of polynomials on the reference element $\mathcal{E}_{\text{ref}}$. Hence, all integrals involving the basis functions can be precomputed, which leads to a quadrature-free semi-discrete formulation. For a detailed derivation of the DG discretisation of the elastic wave equation, see (e.g., Dumbser & Käser 2006).

We employ Arbitrary high-order DERivative (ADER) time stepping (Dumbser et al. 2008; Gassner et al. 2011). This predictor-corrector scheme is particularly suitable for solving hyperbolic PDEs, as it allows time and space discretisation at the same high order. First, an element-local predictor is computed. Based on the predictor values, the numerical flux across element interfaces is computed. In the corrector phase, the numerical fluxes are used to obtain the final solution at the next time step. The ADER-DG scheme achieves the same order of convergence in space and time.

Since the coupling between solid and fluid introduces a stiff source term, we need a locally implicit time-stepping scheme, such as the space-time variant of ADER-DG (e.g., Gassner et al. 2011), which computes the predictor values from an element-local space-time discretisation. de la Puente et al. (2008) demonstrated how the stiff source term in the poroelastic wave equation can successfully be integrated using such a space-time ADER-DG scheme. This requires the solution of a linear system with several hundred unknowns for *each* element update. Recently, Wolf et al. (2022) derived a more efficient approach based on a blockwise back substitution algorithm. We refer to this previous work for verification of the scheme and description of its parallelization and optimization for current supercomputers.

The dynamic rupture (DR) source mechanism can be implemented using numerical fluxes (de la Puente et al. 2009; Pelties et al. 2012a). First, the state Q^* at the interface is computed by solving the Riemann problem, just as in the regular case. The state Q^* is used to evaluate the normal stress and traction at the fault interface. Based on these quantities, we can evaluate the slip rate s across the face (which might be zero if the fault is still locked). With the slip rate present, an imposed state Q^{DR} is computed, which is consistent with the Rankine-Hugoniot jump conditions in the Riemann problem and the friction law. Then, we use $F(Q^-, Q^+) = \tilde{A}_{pq} Q^{\text{DR}}$. More details can be found in Uphoff (2020); Duru et al. (2021).

In order to incorporate dynamic rupture sources in poroelastic media, the pressure-weakening effect has to be taken into account. Here, we summarise the main steps of the approach. More details of the derivation can be found in Appendix B. Again, the state Q^* at the interface has to be found, which is the solution to the Riemann problem at the interface. The solution to the poroelastic Riemann problem has to comply with three wave modes: the fast P-wave, the S-wave, and the slow P-wave Plona (1980). It can be obtained using the Rankine-Hugoniot relations: In the elastic case, the normal stress at the interface σ_n and the traction σ_t are independent of each other. In the poroelastic case, we also have to consider the pressure p^* at the interface, which is tightly coupled to the normal stress. Once the normal stress and the pressure at the interface are available, we consider the effective normal stress $\tilde{\sigma}_n = \sigma_n - p^*$, instead of the normal stress σ_n.

3 RESULTS

3.1 Seismic waves radiated by a double-couple point source in poroelastic media

3.1.1 Verification of the double-couple implementation in a poroelastic homogeneous full space model

If we are interested in seismic waves at teleseismic distances from the hypocentre, the slip at the fault may be approximated by a dislocation at an infinitesimally small fault, i.e., as slip at a point. The seismic wave field radiated by earthquakes can be approximated by the wave field radiated by a double-couple (DC) point source (Aki & Richards 2002). A DC source may be described by a moment tensor $\mathcal{M}$. Wolf et al. (2022) used an explosive point source to verify the ADER-DG scheme for poroelastic media in the open-source software SeisSol. However, the explosive source radiates P-waves only. Therefore, here, we first verify the scheme using a DC point source that radiates both P- and S-waves.

We consider a model of a homogeneous full space similar to that of Wolf et al. (2022), but replace the explosive source with a DC point source. We use the definition of the fault coordinate systems as by Moczo et al. (2014), and consider a source located at the origin with $\Phi_s = \delta = \lambda = 0.0°$, corresponding to $\mathcal{M}_{xz} = \mathcal{M}_{zx} = -1$ being the only non-zero components of the moment tensor. The source time function is a Ricker wavelet with dominant frequency $f_0 = 16\,\mathrm{Hz}$ and time delay $t_0 = 0.07\,\mathrm{s}$. We study two different materials, which only differ in their fluid viscosity. The material parameters (including viscosity ν for a viscous fluid) are given in Table 1. Additionally, we consider an inviscid fluid with viscosity $\nu = 0.0\,\mathrm{Pa\,s}$. We place 12 receivers in the x-z-plane along three different diagonals at angles $0°, 22.5°$ and $45°$ from the x-axis, at distances $600\,\mathrm{m}$, $1{,}000\,\mathrm{m}$, $1{,}800\,\mathrm{m}$ or $3{,}000\,\mathrm{m}$ from the source, respectively, as illustrated in Figure 1.

The 3D mesh spans the volume $[-7\,\mathrm{km}, -7\,\mathrm{km}^3]$. Within a cuboid around the receivers and the source, we specify a characteristic mesh size of $30.0\,\mathrm{m}$ with adaptive refinement towards the source and coarsening towards the boundary. The refinement area is rotated with respect to the domain boundaries such that it symmetrically aligns with the receiver locations (Figure 1). In total, the mesh consists of $47{,}200{,}000$ tetrahedrons. We use 5th degree polynomials, resulting in a convergence order of $\mathcal{O}6$. We computed the numerical solution using 300 nodes of the supercomputer SuperMUC-NG. The reference solution is computed using the semi-analytical solution of Karpfinger et al. (2009).

Table 1. Material parameters for the double-couple point source in a poroelastic homogeneous full space scenario.

Parameter	Value		
ρ_S	2.08	$\times 10^{3}$	$\mathrm{kg\,m^{-3}}$
K_S	2.0	$\times 10^{10}$	Pa
λ_M	5.28	$\times 10^{9}$	Pa
μ_M	6.40	$\times 10^{9}$	Pa
κ	6.00	$\times 10^{-13}$	$\mathrm{m^2}$
T	2		
ϕ	0.4		
ρ_F	1.04	$\times 10^{3}$	$\mathrm{kg\,m^{-3}}$
K_F	2.50	$\times 10^{9}$	Pa
ν	1.0	$\times 10^{-3}$	Pa s

Figure 2 shows a detailed comparison of particle velocity u calculated using SeisSol and the reference solution at a selected receiver 10. To assess the accuracy, we evaluate time-frequency misfits (Kristekova et al. 2006, 2009). The low envelope and phase misfits (EM, PM) indicate very good agreement between the solutions for the inviscid as well as the viscous fluid model setups. We note that the misfits are slightly higher when using the inviscid fluid. In the inviscid case, the slow P-

Figure 1. Receiver positions for the double-couple (DC) point source 3D scenario in the x-z-plane. All receivers are located either 600 m, 1,000 m, 1,800 m or 3,000 m away from the source at 0°, 22.5° and 45° from the x-axis, respectively. The filled black circle indicates the DC source location. The black rectangle shows the area in which the mesh is adaptively refined.

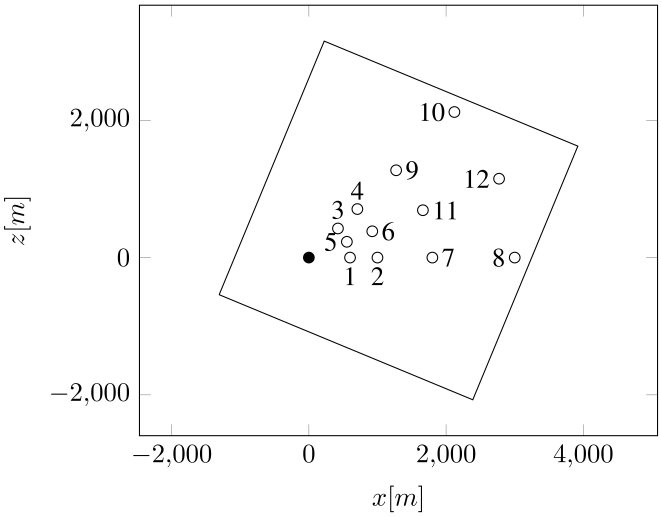

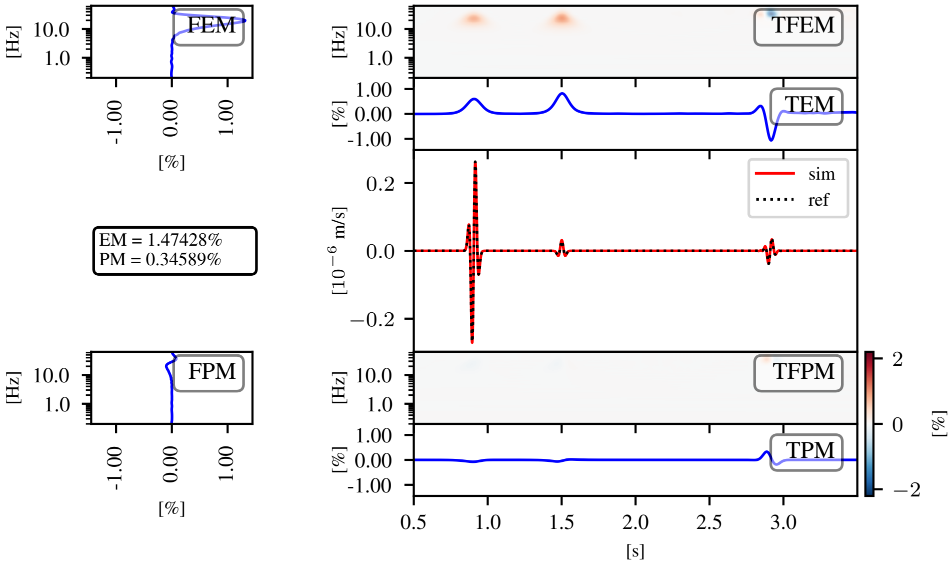

(a) Pores filled with an inviscid fluid.

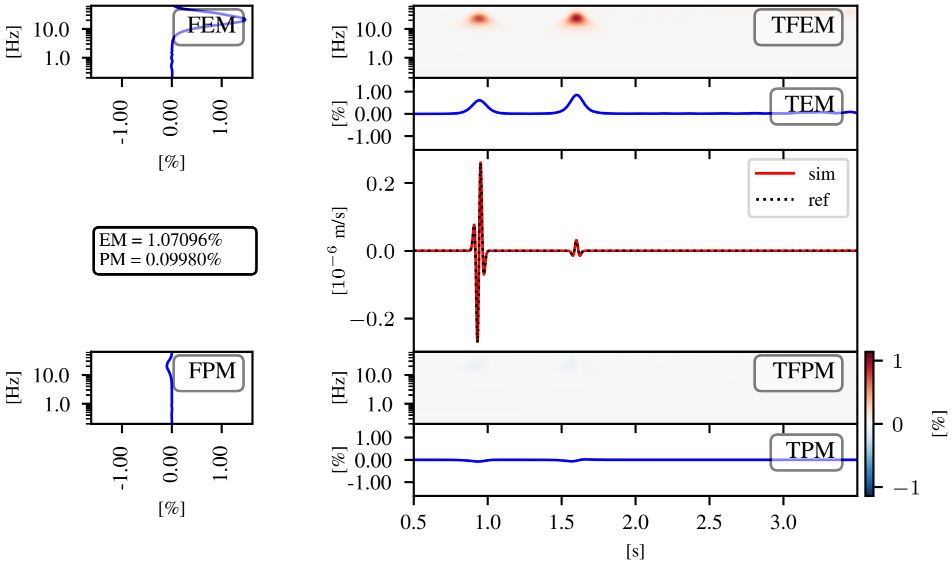

(b) Pores filled with a viscous fluid.

Figure 2. Detailed time-frequency misfit plots for the particle velocity u at receiver `10` in the homogeneous full space test case. The plots show the difference between the numerical SeisSol solution (red) and the semi-analytical reference solution (black dots). We plot several time-frequency misfit criteria (Kristekova et al. 2006, 2009): Frequency Envelope Misfit (FEM), Time-Frequency Envelope Misfit (TFEM), Time Envelope Misfit (TEM), single-valued Envelope Misfit (EM), single-valued Phase Misfit (PM), Frequency-Phase Misfit (FPM), Time-Frequency Phase Misfit (TFPM) and Time-Phase Misfit (TPM).

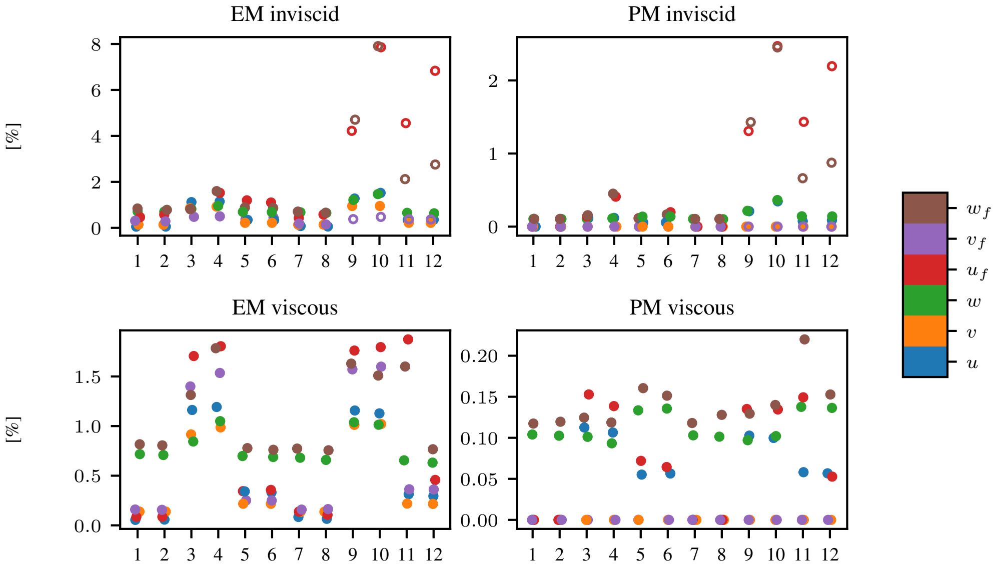

Figure 3. Envelope misfits (EM) and phase misfits (PM) for different quantities (indicated by colours) at all receivers (indicated by numbers at x-axis) in the poroelastic homogeneous full space model setup. Note: The open circles denote non-converged solution components. See the text for a more detailed explanation.

wave is propagating with lower velocity and thus has a shorter wavelength, which renders this case numerically more challenging.

To evaluate the overall accuracy, we show EM and PM values for all three components of particle velocity and relative fluid velocity at all receivers in Figure 3. The EM and PM values of u, w, u_f and w_f are also tabulated in the Appendix (Table A1 and Table A2).

First, let us explain the origin of the rather large EM and PM misfits of up to 8% and 2.5%, respectively, characterising the relative fluid velocities at receivers 9 to 12. In the inviscid case, the slow P-wave is propagating with a wavelength of $26.4\,\mathrm{m}$ at $40\,\mathrm{Hz}$, which approximately matches the maximum frequency of the source time function. The affected receivers are located at a distance of $1{,}800\,\mathrm{m}$ or $3{,}000\,\mathrm{m}$, corresponding to several tens of wavelengths of the slow P-wave. The numerical convergence analysis in Käser et al. (2008) suggests that using two elements per wavelength is required for 5th degree polynomial basis functions in the ADER-DG method to achieve sufficiently accurate results. Thus, to accurately simulate the propagation of the slow P-wave, we would need a mesh with an element size of $13.3\,\mathrm{m}$. With an element size of $30\,\mathrm{m}$, the numerical solution for the slow P-wave is underresolved. We note that we do not observe large EM and PM values at receivers 7 to 8. These are at the same distances from the source as receivers 9 to 12, but owing to the source orientation, they fall in the direction of pure S-wave radiation. Thus, there is no slow P-wave propagating in the direction of receivers 7 to 8, and consequently, the EM and PM misfits are not affected by the underresolved slow P-wave. We did not rerun the simulation with finer resolution because this issue only affects the slow P-wave in the unrealistic inviscid case. Moreover, as can be seen from Figure 2, only relative fluid velocities are affected significantly, but these are challenging to measure observationally. Nevertheless, we included the non-converged cases in Figure 3 for completeness, but using different symbols (open circles).

In summary, we observe a very good agreement between the (converged) SeisSol results and the reference solutions, with EM below $2\,\%$ and PM below $0.5\,\%$.

3.1.2 Verification of the double-couple implementation in a poroelastic layer-over halfspace model

We verified the homogeneous full-space model solution (in section 3.1.1) against a semi-analytical reference solution. However, such a semi-analytical solution is not applicable to a model with internal interfaces or a free surface. Both present important features for realistic numerical simulations of seismic wave propagation in poroelastic materials. Therefore, we next verify our poroelastic ADER-DG scheme in a layer-over-halfspace, model which contains one internal interface and a planar, free surface. Since we are not aware of available (semi-)analytic solutions, we compare our ADER-DG solution with a solution obtained by the finite-difference method (Moczo et al. 2019; Gregor et al. 2022, 2021).

We parameterise a poroelastic layer over a poroelastic halfspace, similar to the 'LOHp' model of Wolf et al. (2022). The layer is $500\,\mathrm{m}$ thick and consists of a softer material with slower wave speeds compared to the halfspace. Atop the slower layer, we impose a free-surface boundary condition. The material parameters for the layer and the half-space are given in Table 2. We specify a DC source with $\Phi_s = 90°, \delta = 22.5°$ and $\lambda = 90°$. Since the slip vector lies in the $x - z$ plane, it allows the creation of a line source by extending the source along the y-axis to enable comparison of the results with a 2D finite-difference solution. We place the source at depth $z = 1{,}010\,\mathrm{m}$. We use a Gabor wavelet with a flat spectrum up to roughly $10\,\mathrm{Hz}$ as the source time function

$$s(t) = \cos(\omega(t - t_0)) \cdot \exp(-(\omega(t - t_0)/\gamma)^2)\,, \tag{4}$$

where $\omega = 2 \cdot \pi \cdot f_0$ and $f_0 = 0.5, \gamma = 0.25, t_0 = 0.25$.

We create an unstructured tetrahedral mesh of the domain spanning $[-10\,\mathrm{km}, 10\,\mathrm{km}]\times[-10\,\mathrm{km}, 10\,\mathrm{km}]\times[-7\,\mathrm{km}, 0\,\mathrm{km}]$. The layer interface at $500\,\mathrm{m}$ depth is explicitly meshed. At the top, we impose a free surface boundary condition, while for all other five boundaries, we impose absorbing boundaries to mimic an unbounded half space. The desired element edge length during the mesh generation is set to $50\,\mathrm{m}$ in the cuboid $[-500\,\mathrm{m}, 2{,}500\,\mathrm{m}] \times [-1{,}500\,\mathrm{m}, 1{,}500\,\mathrm{m}] \times [-1{,}500\,\mathrm{m}, 0\,\mathrm{m}]$ and coarsened towards the boundary to up to $250\,\mathrm{m}$. In addition, we refine the mesh towards the source to a high resolution of up to $10\,\mathrm{m}$ element edge length. To capture the slow P-wave accurately, we further refine the mesh inside the layer and below the interface up to a resolution of $5\,\mathrm{m}$ (i.e., in the region $[-200\,\mathrm{m}, 2{,}200\,\mathrm{m}] \times [-500\,\mathrm{m}, 500\,\mathrm{m}] \times [-550\,\mathrm{m}, 0\,\mathrm{m}]$). The line source is represented by point sources equally spaced with $50\,\mathrm{m}$ distance along the y-axis. The mesh contains $47{,}500{,}000$ tetrahedrons. As before, we use polynomials up to degree 5 as basis functions, to achieve a convergence order of $\mathcal{O}6$. The total simulation time is $2\,\mathrm{s}$. The reference FD solution is computed on a regular uniform grid with $0.625\,\mathrm{m}$ grid spacing.

We record the wave field at a set of receivers placed along a regular grid with lateral distances of 0, 250, 500, and $1{,}000\,\mathrm{m}$ from the source. The complete receiver configuration is depicted in Figure 4: We place the receivers with a spacing of $5\,\mathrm{m}$ between depths of $5\,\mathrm{m}$ and $35\,\mathrm{m}$. To enable a more accurate analysis of the seismic wave field near the free surface, we specify additional receivers at a depth of $0.5\,\mathrm{m}$ and $2.5\,\mathrm{m}$. We also place receivers in the middle of the layer, above and below the interface, and in the halfspace. We do not consider receivers directly at the free surface because, in the FD method, the free-surface boundary condition ($p \equiv 0$) is enforced exactly, whereas, in the DG framework, the free-surface boundary condition is only enforced in a weak sense by imposing a particular flux term. Consequently, pore pressure at the free surface in DG solutions will be small but not obey to $p \equiv 0$. Quantifying the (mis)match between the solutions using a relative error measure (such as the time-frequency misfits) when the reference solution is exactly zero would lead to misleading results.

Above, in section 3.1.1, we have compared the solid velocities and the relative fluid velocities with the reference solution. The relative fluid velocities are important auxiliary quantities for the numerical method and are therefore important for comparing the results of two numerical methods. However,

Table 2. Material parameters for the poroelastic layer-over-halfspace scenario.

Parameter	Halfspace	Layer	
ρ_S	2.50×10^{3}	2.21×10^{3}	$\mathrm{kg\,m^{-3}}$
K_S	40.0×10^{9}	7.60×10^{9}	Pa
λ_M	12.0×10^{90}	3.96×10^{9}	Pa
μ_M	12.0×10^{90}	3.96×10^{9}	Pa
κ	6.00×10^{-12}	1.00×10^{-12}	$\mathrm{m^2}$
T	2	2	
ϕ	0.20	0.16	
ρ_F	1.04×10^{3}	1.04×10^{3}	$\mathrm{kg\,m^{-3}}$
K_F	2.5×10^{9}	2.5×10^{9}	Pa
ν	1.0×10^{-3}	1.0×10^{-3}	$\mathrm{Pa\,s}$

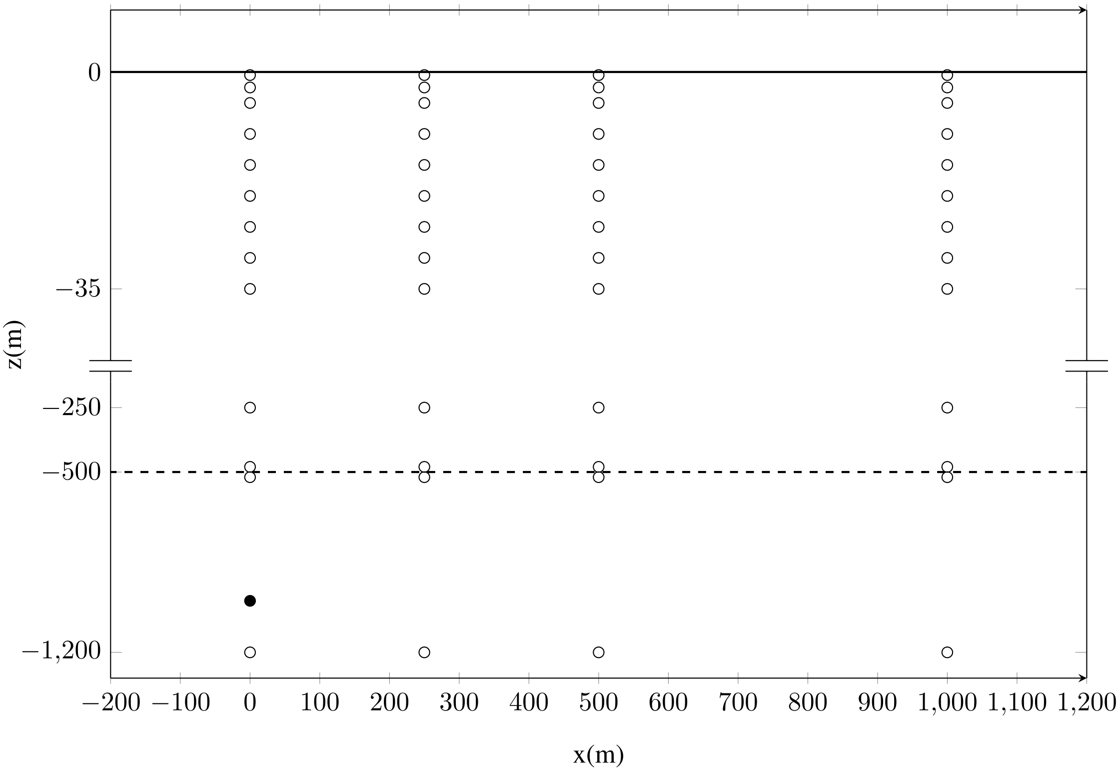

Figure 4. Receiver positions (circles) for the poroelastic layer-over-halfspace scenario. The thick black line at $z = 0\,\mathrm{m}$ represents the location of the free surface, and the dashed line represents the location of the material interface. The filled black circle denotes the double-couple source position. Note that the z-axis contains a break and uses a zoomed-in scale above the break.

because they quantify the relative motion of the fluid in the pore space with respect to the motion of the matrix, they can hardly be observed in reality. In the previous section, we have concentrated on the relative fluid velocities. The analytic reference solution only provided the displacement of the matrix together with the relative fluid motion. The more relevant quantity with practical implications is the fluid pressure. Consequently, we will focus on the evaluation of solid velocities and fluid pressure from now on.

Figure 5 summarizes the envelope misfits for x- and z-components of particle velocities, u and w, and pore fluid pressure p. If we consider the receivers at $2.50\,\mathrm{m}$ depth and below, we find that the envelope misfits are well below $3\,\%$. For the near-surface receivers (depth of $0.5\,\mathrm{m}$), we observe very small envelope misfits (EM) for particle velocities, consistently with the small EM values for deeper receivers. However, for pore pressure, we observe much larger EM values. All phase misfits are well below $1.5\,\%$.

To explain the partially elevated EM values, let's have a closer look at the depth-dependent evolution of pore pressure near the free surface. Figure 6 shows the pore pressure time histories at

$x = 1{,}000\,\mathrm{m}$ recorded at different receiver depths. First, we see that the pore pressure at the free surface (blue line) is visually zero, as expected and explained above. Second, the magnitude of pore pressure does not significantly vary for depths between $2.5\,\mathrm{m}$ and $30\,\mathrm{m}$. This implies that the transition of pore pressure from $0\,\mathrm{Pa}$ at the free surface to $\sim 30\,\mathrm{Pa}$ must occur within the top $2.5\,\mathrm{m}$. Capturing such steep variations of pore pressure is inherently challenging for elements with an edge length of $5\,\mathrm{m}$. We recall that the reference FD solution is obtained with a grid spacing of $0.625\,\mathrm{m}$. From Figure 5, we can conclude that the overall agreement is good. However, if high accuracy in modelled pore pressure near the free surface is important, the use of even smaller element sizes is inevitable.

Figure 7 shows the distribution of pore pressure for the poroelastic layer-over-halfspace model. Due to the steep increase of pore pressure near the free surface (depicted in Figure 6), we cannot see zero pore pressure at the free surface (the top edge of the plot). We also observe an apparent discontinuity in pore pressure at the internal interface. The explanation of this effect is similar to that of the free-surface effect. Pore pressure variations near the internal interface are too steep to be captured at this scale.

3.1.3 Application to the Sleipner, Utsira, carbon capture and storage site

In this section, we apply SeisSol to model seismic wave propagation in a realistic 3D poroelastic model of a carbon capture and storage (CCS) site, Sleipner, which is a part of the larger Utsira Formation, a deep saline reservoir located $800\,\mathrm{m}$ to $1{,}000\,\mathrm{m}$ below the sea floor off the coast of Norway.

First, we briefly describe the procedure for developing the computational model: We define a complex 3D geometry of interfaces separating sandstone layers by impermeable shale layers from the Sleipner 2019 benchmark model (Equinor 2019). For a complete characterization of a poroelastic material, we need ten parameters. However, such a detailed description of the materials is not available neither for the Sleipner site nor the Utsira formation. We, therefore, derive the missing material parameters as described in the following: First, we use P-wave velocities for the Utsira formation reported by Yan (2017), who further refers to Traub (2008). Based on the P-wave speed values, we associate individual layers with one of five poroelastic materials: caprock, sandstone, thick shale, intra-shale, and bedrock. Additionally, we consider a roughly $700\,\mathrm{m}$ thick, effectively elastic layer above the caprock.

Figure 8 depicts the overall structure of our model. The S-wave speeds are calculated from the respective P-wave speeds using empirical relations by Vernik et al. (2002) and Mavko et al. (2009). These empirical relations distinguish between brine-saturated sandstones and shales. Therefore, we use these relations for the sandstone material and all shale materials (including caprock and bedrock), respectively. Density is determined by the power-law form of Gardener's empirical relation, with coefficients for sandstone (Gardner et al. 1974; Castagna & Backus 1993; Mavko et al. 2009) consistently

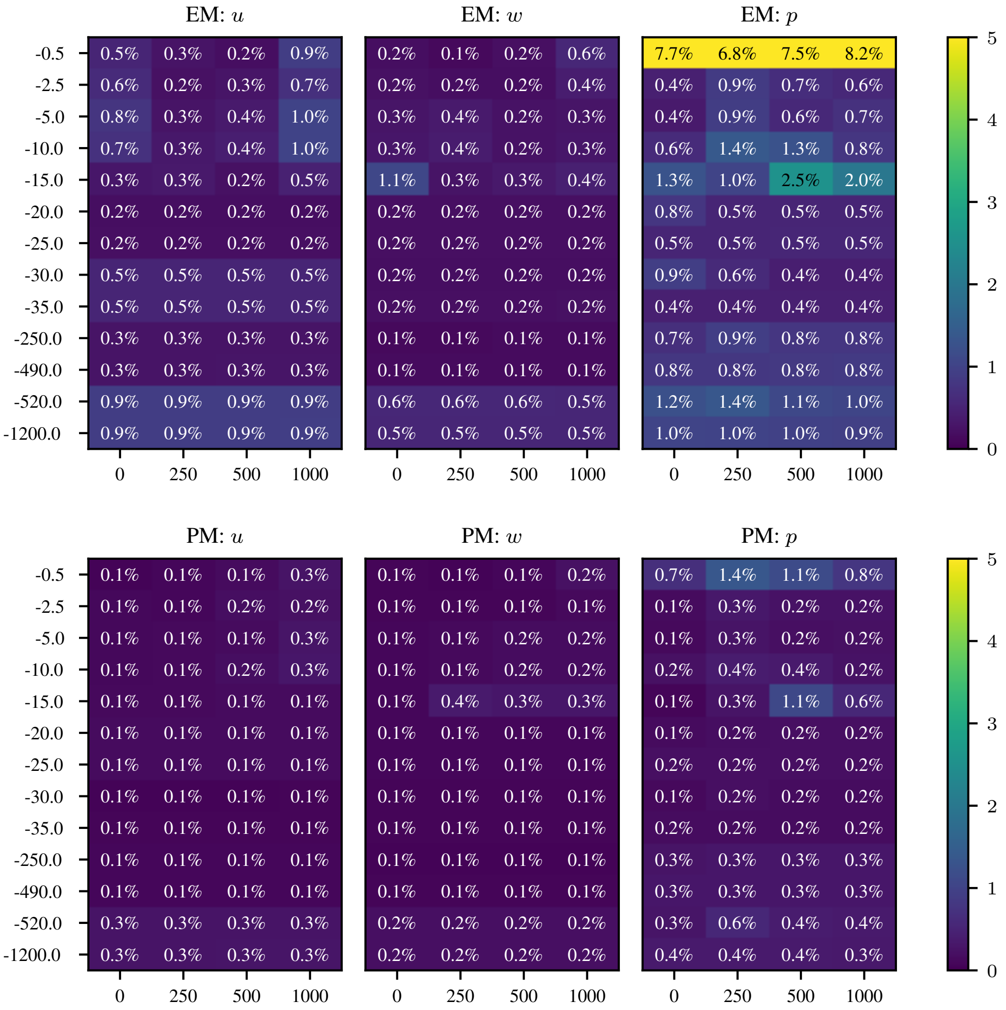

	EM: u				EM: w				EM: p			
	0	250	500	1000	0	250	500	1000	0	250	500	1000
-0.5	0.5%	0.3%	0.2%	0.9%	0.2%	0.1%	0.2%	0.6%	7.7%	6.8%	7.5%	8.2%
-2.5	0.6%	0.2%	0.3%	0.7%	0.2%	0.2%	0.2%	0.4%	0.4%	0.9%	0.7%	0.6%
-5.0	0.8%	0.3%	0.4%	1.0%	0.3%	0.4%	0.2%	0.3%	0.4%	0.9%	0.6%	0.7%
-10.0	0.7%	0.3%	0.4%	1.0%	0.3%	0.4%	0.2%	0.3%	0.6%	1.4%	1.3%	0.8%
-15.0	0.3%	0.3%	0.2%	0.5%	1.1%	0.3%	0.3%	0.4%	1.3%	1.0%	2.5%	2.0%
-20.0	0.2%	0.2%	0.2%	0.2%	0.2%	0.2%	0.2%	0.2%	0.8%	0.5%	0.5%	0.5%
-25.0	0.2%	0.2%	0.2%	0.2%	0.2%	0.2%	0.2%	0.2%	0.5%	0.5%	0.5%	0.5%
-30.0	0.5%	0.5%	0.5%	0.5%	0.2%	0.2%	0.2%	0.2%	0.9%	0.6%	0.4%	0.4%
-35.0	0.5%	0.5%	0.5%	0.5%	0.2%	0.2%	0.2%	0.2%	0.4%	0.4%	0.4%	0.4%
-250.0	0.3%	0.3%	0.3%	0.3%	0.1%	0.1%	0.1%	0.1%	0.7%	0.9%	0.8%	0.8%
-490.0	0.3%	0.3%	0.3%	0.3%	0.1%	0.1%	0.1%	0.1%	0.8%	0.8%	0.8%	0.8%
-520.0	0.9%	0.9%	0.9%	0.9%	0.6%	0.6%	0.6%	0.5%	1.2%	1.4%	1.1%	1.0%
-1200.0	0.9%	0.9%	0.9%	0.9%	0.5%	0.5%	0.5%	0.5%	1.0%	1.0%	1.0%	0.9%

	PM: u				PM: w				PM: p			
	0	250	500	1000	0	250	500	1000	0	250	500	1000
-0.5	0.1%	0.1%	0.1%	0.3%	0.1%	0.1%	0.1%	0.2%	0.7%	1.4%	1.1%	0.8%
-2.5	0.1%	0.1%	0.2%	0.2%	0.1%	0.1%	0.1%	0.1%	0.1%	0.3%	0.2%	0.2%
-5.0	0.1%	0.1%	0.1%	0.3%	0.1%	0.1%	0.2%	0.2%	0.1%	0.3%	0.2%	0.2%
-10.0	0.1%	0.1%	0.2%	0.3%	0.1%	0.1%	0.2%	0.2%	0.2%	0.4%	0.4%	0.2%
-15.0	0.1%	0.1%	0.1%	0.1%	0.1%	0.4%	0.3%	0.3%	0.1%	0.3%	1.1%	0.6%
-20.0	0.1%	0.1%	0.1%	0.1%	0.1%	0.1%	0.1%	0.1%	0.1%	0.2%	0.2%	0.2%
-25.0	0.1%	0.1%	0.1%	0.1%	0.1%	0.1%	0.1%	0.1%	0.2%	0.2%	0.2%	0.2%
-30.0	0.1%	0.1%	0.1%	0.1%	0.1%	0.1%	0.1%	0.1%	0.1%	0.2%	0.2%	0.2%
-35.0	0.1%	0.1%	0.1%	0.1%	0.1%	0.1%	0.1%	0.1%	0.2%	0.2%	0.2%	0.2%
-250.0	0.1%	0.1%	0.1%	0.1%	0.1%	0.1%	0.1%	0.1%	0.3%	0.3%	0.3%	0.3%
-490.0	0.1%	0.1%	0.1%	0.1%	0.1%	0.1%	0.1%	0.1%	0.3%	0.3%	0.3%	0.3%
-520.0	0.3%	0.3%	0.3%	0.3%	0.2%	0.2%	0.2%	0.2%	0.3%	0.6%	0.4%	0.4%
-1200.0	0.3%	0.3%	0.3%	0.3%	0.2%	0.2%	0.2%	0.2%	0.4%	0.4%	0.4%	0.3%

Figure 5. Envelope and Phase misfits between the SeisSol DG solution and the finite difference (FD) reference solution at receiver points in the poroelastic layer-over-halfspace model. Compare to Figure 4 for a sketch of the source-receiver configuration. Except for the pressure close to the free surface, we find excellent agreement between the DG simulation results and the FD reference solution.

with Yan (2017). The estimated values of P- and S-wave speeds and density are given in Table 3. We use them as the input to our rock physics inversion, which is based on a nearest-neighbour algorithm utilizing Voronoi cell sampling (Sambridge 1999; Dupuy et al. 2016).

To better constrain the inversion, we fix values of fluid bulk modulus, fluid density, and viscosity, assuming the pore space is filled with brine. To further help constrain the inversion, we also assume a-priori values of solid bulk modulus K_S, solid density ρ_S, and permeability κ. Yan (2017) provided values of the three parameters for sandstone and bedrock in the Utsira formation, but we assume that all shale layers (thick shale, intra-shales, caprock, and bedrock) have the same properties regarding K_S, ρ_S and κ. Since we find that the inversion very poorly constrains tortuosity, we use a fixed value

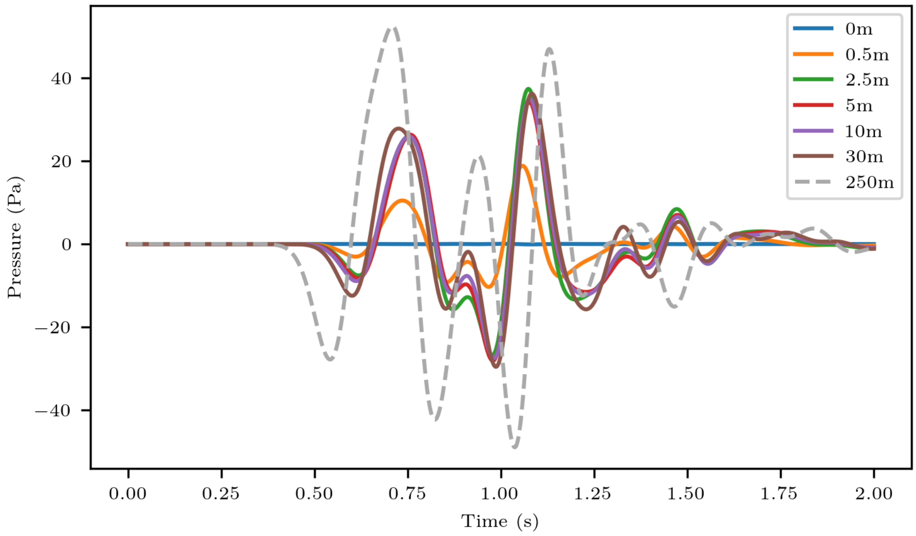

Figure 6. Time history of the pressure at $x = 1{,}000\,\mathrm{m}$ for different receiver depths in the poroelastic layer-over-halfspace SeisSol DG simulation. The pressure at $z = 0\,\mathrm{m}$ is zero, reflecting the traction-free boundary condition. Already at a depth of $z = 0.5\,\mathrm{m}$, we observe a pressure field at roughly half the amplitude compared to a depth of $z = 250\,\mathrm{m}$. This highlights the steep pressure gradient towards interfaces.

for the tortuosity of all materials in our model. Subsequently, the rock physics inversion is used to find the values of elastic moduli of the matrix and porosity.

SeisSol currently does not support combining elastic and poroelastic materials in one computational simulation. Therefore, instead of parameterising an elastic layer above the caprock, we use a

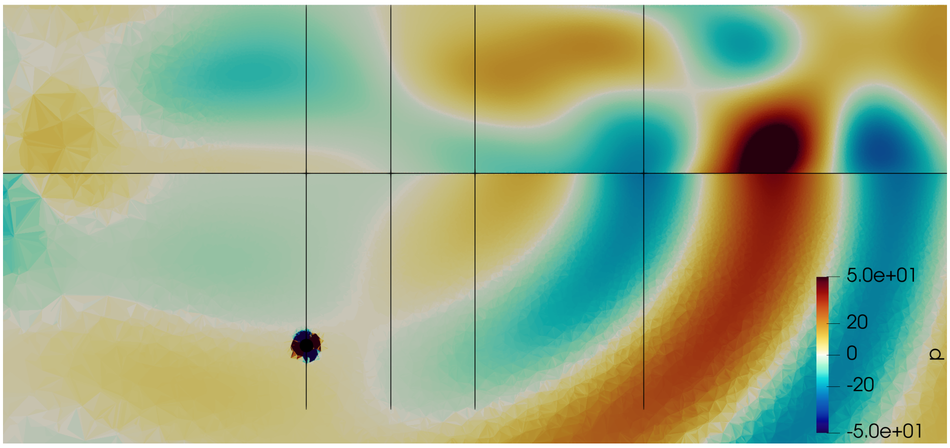

Figure 7. Snapshot of the pressure field at $1.3\,\mathrm{s}$. Black lines denote the lines of receivers at $x = 0\,\mathrm{m}$, $250\,\mathrm{m}$, $500\,\mathrm{m}$ and $1{,}000\,\mathrm{m}$ as well as the interface at $500\,\mathrm{m}$ depth. The black circle denotes the position of the DC source. At this scale, the pressure appears to be discontinuous across the interface. See also Figure 6 for a detailed overview of the pressure field at an interface.

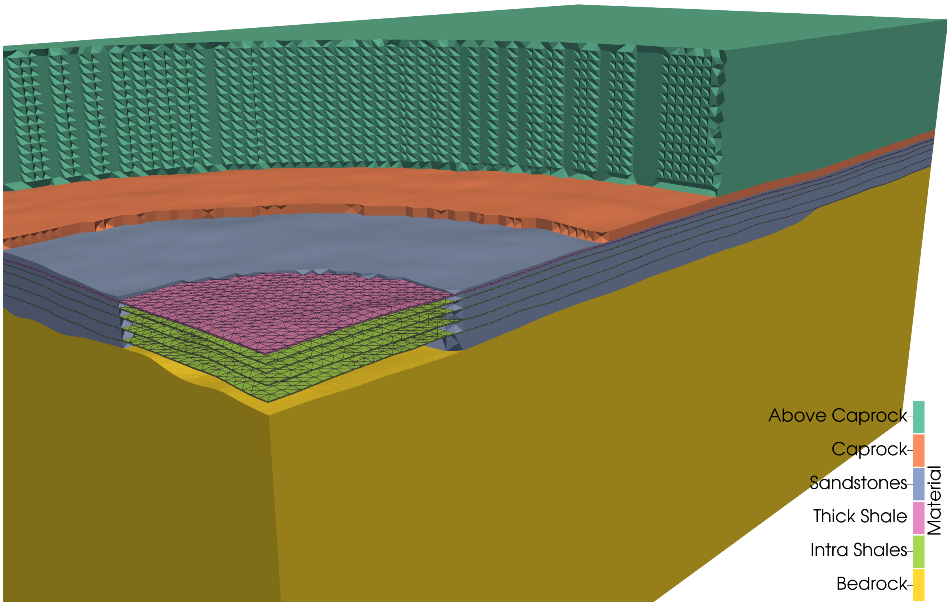

Figure 8. View of the unstructured tetrahedral mesh adapted from the geometrically complex 3D Sleipner, Utsira CCS site. To clearly illustrate the different layers and how they are geometrically represented in the mesh in this figure, the mesh resolution is lower than for the mesh that is used for the numerical simulations with SeisSol. The mesh shown in this figure contains $6{,}790{,}000$ elements, while the fine mesh used in the simulations contains $65{,}000{,}000$ elements.

poroelastic material with negligible poro-elastic effects, that effectively behaves as elastic material. All poroelastic material parameters for all materials in the computational model are summarised in Table 4. Note that except for the sandstone layers, all other layers are almost impermeable.

The thickness of some intra-shale layers in the original model is only $1\,\mathrm{m}$ to $2\,\mathrm{m}$, which is very small compared to the wavelengths expected in the model for a dominant frequency of $16\,\mathrm{Hz}$ (tens of meters). Therefore, to facilitate the meshing process, we modified the original model such that all layers are at least $5\,\mathrm{m}$ thick. To avoid intersections of these thicker layers, we also removed some of the intra-shale layers. The area of interest, including the complex geometry and interfaces, spans $[0\,\mathrm{m}, 3{,}200\,\mathrm{m}] \times [0\,\mathrm{m}, 5{,}900\,\mathrm{m}]$. To minimize potential artificial reflections from the absorbing boundaries, we enlarge the mesh to the area $[-5{,}000\,\mathrm{m}, 8{,}000\,\mathrm{m}] \times [-5{,}000\,\mathrm{m}, 11{,}000\,\mathrm{m}]$ and to a depth of $6{,}500\,\mathrm{m}$. We enforce a characteristic edge length of $10\,\mathrm{m}$ in the bulk and $5\,\mathrm{m}$ in the thinnest layers, resulting in a mesh with $65{,}000{,}000$ tetrahedrons. Again, polynomials up to degree 5 are used as basis functions.

The geometric flexibility of the DG method allows us to explicitly represent the layer interfaces in the inner mesh, where the 3D geometry of the layers is available. Outside this area, we infer a 1D depth-dependent material model. Therefore, we compute the average depth of each interface and enforce a planar interface outside the area, where detailed layer information is available. The characteristic edge length for the tetrahedral mesh generation is set to $5\,\mathrm{m}$ in order to align with the thickness of the shale layers. A lower resolution version of the resulting mesh is shown in Figure 8.

We consider a double-couple point source with $\Phi_s = 90.0°, \delta = 90.0°$ and $\lambda = 0.0°$ with its hypocentre at $(x, y, z) = (1{,}500\,\mathrm{m}, 3{,}000\,\mathrm{m}, 1{,}500\,\mathrm{m})$. The source time function is a Ricker wavelet with a dominant frequency of $f_0 = 16\,\mathrm{Hz}$, which is identical to the verification setup in the poroelastic homogeneous full-space model. We record the seismic wave field at a line of receivers at $x = 1{,}750\,\mathrm{m}$, $y = 3{,}750\,\mathrm{m}$ and $z = 0\,\mathrm{m}, 5\,\mathrm{m}, \ldots, 2{,}000\,\mathrm{m}$.

We compare the poroelastic version of the model to the elastic equivalent, using the Gassmann approximation (Carcione 2015; Gassmann 1951). Figure 9 shows the envelope misfits (EM) for solid particle velocities between poroelastic and equivalent elastic models. The EM values remain consistently below $0.5\,\%$ throughout the domain, which implies that both models essentially yield the same deformation of the matrix. However, this interpretation ignores the effect of pore pressure.

The pressure of pore fluids is only explicitly modeled using the poroelastic model. In the Gassmann equivalent elastic model, the total stress σ is the sum of the fluid pressure p and the stress sustained by the matrix $\tilde{\sigma}$, but fluid pressure is not readily quantifiable. In the sandstone layers, the fluid pressure can account for up to two-thirds of the total stress. The fault strength depends on the stress sustained by the matrix $\tilde{\sigma}$ only. Thus, the correct computation of the fluid pressure is vital to assess, for example, whether dynamic triggering of an earthquake may occur.

We conclude that for poroelastic seismic wave propagation scenarios where only the displacement of the solid matrix is of interest, the Gassmann equivalent is a sufficient approximation. This includes, for example, ground motion estimates from kinematic earthquake source models. However, in the next section, we will study fault interaction in dynamic rupture earthquake models in poroelastic media, for which the fluid pressure can have a significant impact on the dynamic rupture nucleation, propagation, and arrest (e.g., Kammer et al. 2024). In these cases, the Gassmann equivalent approximation can lead to misleading conclusions.

Table 3. Estimated P-wave speed (V_P), S-wave speed (V_S) and density (ρ) for the subsurface materials in the Sleipner, Utsira CCS site model that we use as an input for a rock physics inversion.

Parameter	Above Caprock	Caprock	Sandstones	Thick Shale	Intra Shales	Bedrock	
V_P	1,900	2,300	2,050	2,250	2,150	2,490	$\mathrm{m\,s^{-1}}$
V_S	711	900	589	858	773	1,040	$\mathrm{m\,s^{-1}}$
ρ	2,080	2,060	2,000	2,050	2,030	2,230	$\mathrm{kg\,m^{-3}}$

Table 4. Poroelastic material parameters for the modified Sleipner, Utsira CCS site computational model.

Parameter	Above Caprock	Caprock	Sandstones	Thick Shale	Intra Shales	Bedrock	
K_S	37.0×10^9	22.6×10^9	32.3×10^9	22.6×10^9	22.6×10^9	22.6×10^9	Pa
ρ_S	2.02×10^3	2.39×10^3	2.66×10^3	2.39×10^3	2.39×10^3	2.39×10^3	$\mathrm{kg\,m^{-3}}$
λ_M	5.20×10^9	1.89×10^9	2.81×10^9	1.65×10^9	1.21×10^9	2.91×10^9	Pa
μ_M	1.01×10^9	1.67×10^9	0.695×10^9	1.51×10^9	1.21×10^9	2.29×10^9	Pa
κ	1.00×10^{-21}	1.47×10^{-17}	2.00×10^{-12}	1.47×10^{-17}	1.47×10^{-17}	1.47×10^{-17}	m^2
T	3.0	1.0	1.0	1.0	1.0	1.0	
ϕ	0.02	0.24	0.4	0.25	0.27	0.21	
ρ_F	1.2	1.03×10^3	1.03×10^3	1.03×10^3	1.03×10^3	1.03×10^3	$\mathrm{kg\,m^{-3}}$
K_F	101×10^3	2.3×10^9	2.3×10^9	2.3×10^9	2.3×10^9	2.3×10^9	Pa
ν	1.9×10^{-4}	6.9×10^{-4}	6.9×10^{-4}	6.9×10^{-4}	6.9×10^{-4}	6.9×10^{-4}	Pa s

3.2 3D dynamic rupture in poroelastic media

Dynamic rupture models combine frictional failure along the fault and seismic wave propagation in the surrounding rock volume. In this section, we will extend 3D dynamic rupture simulations with SeisSol to poroelastic materials and present two scenarios in which the incorporation of poroelastic materials significantly changes rupture dynamics. We here study the dynamic effects of poroelasticity

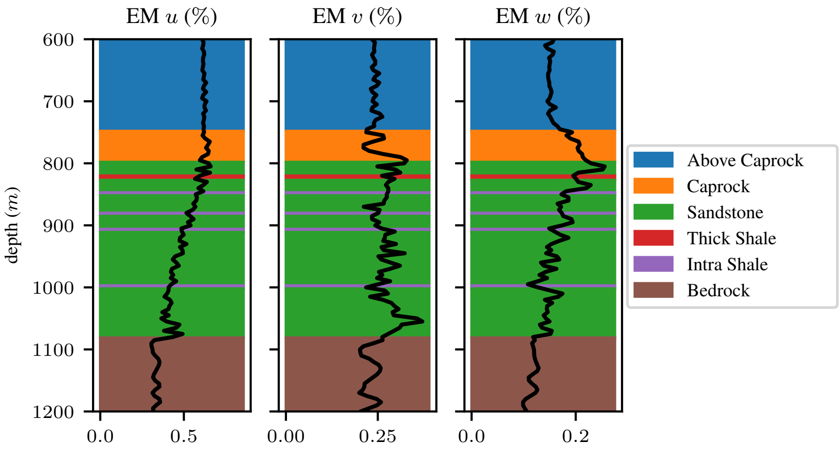

Figure 9. Comparison of the displacement of the elastic matrix between the true poroelastic material and the Gassmann equivalent in the Seipner, Utsira CCS site SeisSol simulations. For all three velocity components, we compute the envelope misfit for receivers placed at $x = 1{,}750\,\mathrm{m}$, $y = 3{,}750\,\mathrm{m}$ with a vertical distance of $5\,\mathrm{m}$. We focus on the sandstone-shale formation between $600\,\mathrm{m}$ and $1{,}200\,\mathrm{m}$ depth. With misfits well below $1\,\%$, we conclude that the true poroelastic material and the Gassmann equivalent yield similar results.

in 3D multi-fault rupture branching and poroelastic fault zone models, paying special attention to the undrained pore pressure changes and their impact on fault strength and rupture propagation.

Previous studies have shown that a critical aspect of modelling dynamic fault strength in poroelastic media is determining the fault pore pressure, which directly influences the effective normal stress and consequently the rupture process of sub- and supershear ruptures (Rudnicki & Rice 2006; Dunham & Rice 2008; Song & Rudnicki 2017; Jha & Juanes 2014; Yang & Juanes 2018; Heimisson et al. 2021; Pampillón et al. 2023; Li & Zhang 2023). Pressure changes across the fault surface depend on the assumed poroelastic parameters and may be discontinuous and antisymmetric, with fluid flow and fault permeability determining the pressure distribution. The short time scales of dynamic rupture simulations account for undrained pore pressure changes, which predominantly affect the effective normal stress. Pore pressure is only uniquely determined when accounting for the continuous fluid flow at the mm-scale in the fault normal direction. However, accurately determining pore pressure on the fault remains challenging, particularly given that small-scale processes such as dilatancy and compaction are not fully constrained at seismogenic depths. Therefore, simplified approaches were considered to account for the pore-pressure effects at the fault. Assuming that the fault is completely impermeable with slip occurring just on one side of the impermeable seal, the fault strength can be determined by using pressure changes on that side. Alternatively, the strength can be determined on both sides of the fault (taking into account pore-pressure on each side) and the fault strength is then selected as the weaker strength. Another approach is to average the pore-pressure values at each side of the fault and then determine the fault strength. However, these simplified approaches lead to radically different predictions on rupture dynamics.

Dynamic rupture models have been implemented in various computational methods that have been established to solve the elastic wave equations, including Finite Differences, Finite Elements, Finite Volumes, Discontinuous Galerkin (DG) methods (e.g., Day 1982; Cruz-Atienza & Virieux 2004; Ely et al. 2009; Zhang et al. 2014; Barall 2009; Aagaard et al. 2013; Uphoff 2020). For dynamic rupture simulations using the ADER-DG approach, a Riemann problem is solved to obtain the traction and velocity values at the fault interface (de la Puente et al. 2008; Pelties et al. 2012b; Duru et al. 2021). Then, the slip rate is computed to be consistent with the friction law and the surrounding elastodynamic wave field. Based on the slip rate, an imposed state at the interface is calculated, which is used in the flux computation later on. In order to combine poroelastic media and dynamic rupture, the solver for the Riemann problem needs to be adapted to take the fluid pressure into account. When the fluid pressure p and the stress in normal direction σ_n at the fault are known, we can compute the effective stress as $\tilde{\sigma} = \sigma_n - p$ (see section 2.2). In our model, we choose the fluid pressure p to be the average of the fluid pressure on both sides of the fault.

3.2.1 *3D rupture dynamics across branching faults in poroelastic materials*

We examine how poroelastic materials influence dynamic rupture across a branching multi-fault geometry. We consider a homogeneous half-space with a vertical planar fault. The main fault is defined as the plane $[-16{,}000\,\mathrm{m}, 12{,}000\,\mathrm{m}] \times \{0\} \times [-15{,}000\,\mathrm{m}, 0\,\mathrm{m}]$. At $x = 0$, the branch segment intersects the main fault. The branch has the same width as the main fault and is $12\,\mathrm{km}$ long. The angle between the branch and the main fault is $15°$. The resulting fault geometry is depicted in Figure 10.

This 3D model setup is similar to the TPV24 scenario (Harris et al. 2009), but the branching angle has been reduced, and the branch is located on the other side of the main fault. We modified the original TPV24 benchmark scenario to investigate the weakening effect of the fluid pressure. In the original configuration, the branch is located in a region of reduced pore-fluid pressure induced by the propagating rupture, thus inhibiting further rupture propagation on the branch. In our modification, the branch is located in the region of increased pore-fluid pressure, allowing us to investigate whether increased pore pressure facilitates dynamic rupture propagation. We performed several trial-and-error simulations with varying branching angles. We chose the scenario with the most pronounced effect of poroelastic rheology.

We consider a uniform background stress tensor

$$\sigma = \begin{pmatrix} -1.70 \times 10^7 & 4.5\ \ \times 10^6 & 0.0 \\ 4.5\ \ \times 10^6 & -1.00 \times 10^7 & 0.0 \\ 0.0 & 0.0 & -1.00 \times 10^7 \end{pmatrix} \mathrm{Pa} \tag{5}$$

and employ linear slip weakening friction with $\mu_s = 0.7, \mu_d = 0.3, D_c = 0.1\,\mathrm{m}$. To suppress supershear transition at the free surface, we set the cohesion at the free surface to $C = 1\,\mathrm{MPa}$, which linearly

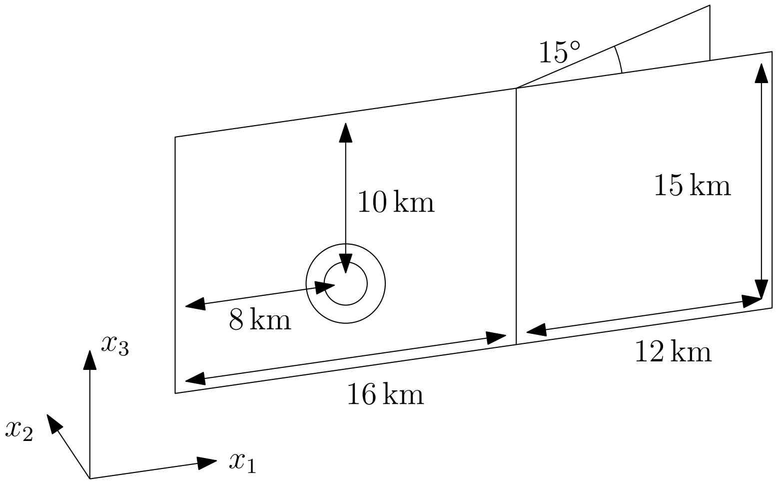

Figure 10. Sketch of the fault geometry for the fault branching experiment. The two circles on the main fault represent the nucleation area. The top of the fault aligns with the free surface.

decreases to 0 at a depth of $1{,}000\,\mathrm{m}$. Below, the cohesion is 0. We initiate the rupture by prescribing local fluid overpressure lowering the effective normal stress:

$$p_0 = \exp\left(-1 \times 10^{-6}\left((x+8000)^2 + (y+500)^2 + (z+10000)^2\right)\right) \cdot 8.0\,\mathrm{MPa}. \tag{6}$$

This distribution approximately corresponds to pore pressure diffusion from a point injection.

We consider the material parameters used by Pampillón et al. (2023) (Table S2 in Supplementary Material), see Table 5. The *SeisSol* parameters can be obtained using these relations: $\mu_M = \frac{E}{2(1+\nu_P)}$, $\lambda_M = \frac{E\cdot\nu_P}{(1+\nu_P)\cdot(1-2\nu_P)}$, $K_M = \lambda_M + \frac{2}{3}\mu_M$, $K_S = \frac{K_M}{1-\alpha_B}$, and $K_F = \frac{1}{\beta}$.

To investigate the role of poroelastic material on rupture propagation, we considered varying values of the Biot coefficient α. Additionally, we also consider the Gassmann equivalent elastic material. Because the Gassmann equivalent material neglects all fluid effects, we use a modified normal stress $\tilde{\sigma} = \sigma_{yy} - p_0$ to nucleate the rupture.

For the numerical simulation of the behaviour at the branch, we embed the fault in the cuboid $[-26{,}000\,\mathrm{m}, 22{,}000\,\mathrm{m}] \times [-10{,}000\,\mathrm{m}, 13{,}100\,\mathrm{m}] \times [-25{,}000\,\mathrm{m}, 0\,\mathrm{m}]$. At $z = 0\,\mathrm{m}$, we impose a free surface boundary condition, all other boundaries are absorbing. This domain is designed ensuring such that each point on the fault system is at least $10\,\mathrm{km}$ away from an absorbing boundary. We chose a mesh resolution of $100\,\mathrm{m}$, which has proven to be sufficiently accurate in a previous convergence test (Wolf 2024). The scenario does not contain any material interfaces, so we do not expect pressure discontinuities (off the faults) as in section section 3.1.2 The final mesh contains 2,300,000 elements. As before, we use polynomials up to degree 5 as basis function.

Figure 11 shows a comparison of the on-fault rupture dynamics and the seismic wave field after $11\,\mathrm{s}$ simulation time using the highest and lowest considered values of α, respectively. On the fault, the colour depicts the friction coefficient. In the purple areas, the friction coefficient is still at its

Table 5. Generic material parameters for the dynamic rupture fault branching experiment

Parameter	Description	Value	
E	Young's modulus	20.0×10^9	Pa
ν_P	Poisson ratio	0.25	
ρ_S	solid density	2.50×10^3	$\mathrm{kg\,m^{-3}}$
ρ_F	fluid density	1.00×10^3	$\mathrm{kg\,m^{-3}}$
ν	fluid viscosity	0.001	$\mathrm{Pa\,s}$
κ	permeability	1.00×10^{-14}	$\mathrm{m^2}$
β	fluid compressiblity	2.00×10^{-9}	$\mathrm{Pa^{-1}}$
ϕ	porosity	0.1	
α	Biot coefficient	0.3	up to 0.9

initial (static) value, i.e., the fault has not broken there. In the yellow areas, the friction coefficient has reduced to 0.3, the dynamic friction coefficient, i.e., the fault has entirely weakened. The figure reveals that rupture jumps onto the branching fault in poroelastic material with $\alpha = 0.9$. In contrast, for the elastic equivalent material, only the main fault breaks and the branch is not activated. For $\alpha = 0.3$, poroelastic material and equivalent elastic material yield the same results, i.e., the rupture does not propagate to the branch.

The Biot coefficient defines the partitioning of the total stress between the solid matrix and the pore fluid (e.g. De Simone et al. 2023). $\alpha = 0$ implies that the external stress results in no increase in pore pressure, and $\alpha = 1$ means that the external stress is equally partitioned between the stress applied to the solid matrix and pore pressure. To better understand the influence of the Biot coefficient, we perform a series of simulations for α ranging between 0.3 and 0.9 in steps of 0.05. This range covers the typically values of α (Detournay & Cheng 1993). We find that for $\alpha < 0.75$, the poroelastic and the Gassmann equivalent materials yield consistent results. However, for $\alpha \geq 0.75$, the results deviate. In the poroelastic case, both faults, the main fault and the branch, break, but in the elastic equivalent material only the main fault breaks.

In the elastic equivalent material, the branch never breaks in our simulations, whereas in the poroelastic material it breaks, if the Biot coefficient is sufficiently high. This implies that for high values of α, the elastic equivalent material is not a sufficient approximation of the full poroelastic behaviour. In the case of a low Biot coefficient, though, we do not see a qualitative difference between the poroelastic material and its elastic equivalent. At the same time, it is important to note that the response of poroelastic material does not depend on the Biot coefficient only, and, therefore, $\alpha = 0.75$ is not a universal threshold for applicability of the elastic equivalent material for rupture dynamics.

Additionally, this effect is recognizable in the release of seismic energy. We plot the on-fault measured seismic moment rate for all four scenarios in Figure 12. For $\alpha = 0.3$, the moment release rate is almost identical, when comparing the poroelastic and elastic materials. For $\alpha = 0.9$, the picture is very different. The moment release rate for the elastic version remains consistent with that for $\alpha = 0.3$ (it is, in fact, slightly lower). However, in the poroelastic version, we observe an additional increase in seismic moment rate after around $5\,\mathrm{s}$, corresponding to the simulation time when the rupture jumps onto the branch.

Finally, we briefly mention our analysis using poroelastic properties corresponding to real-world materials in (Detournay & Cheng 1993; Li & Zhang 2023) instead of generic material paramters (see Table 6). As expected, for all elastic equivalent material, only the main fault breaks and the branch remains intact. For charcoal granite (with very low α of 0.222), the elastic equivalent and poroelastic materials yield consistent results. However, for all other materials, we observe that for poroelastic

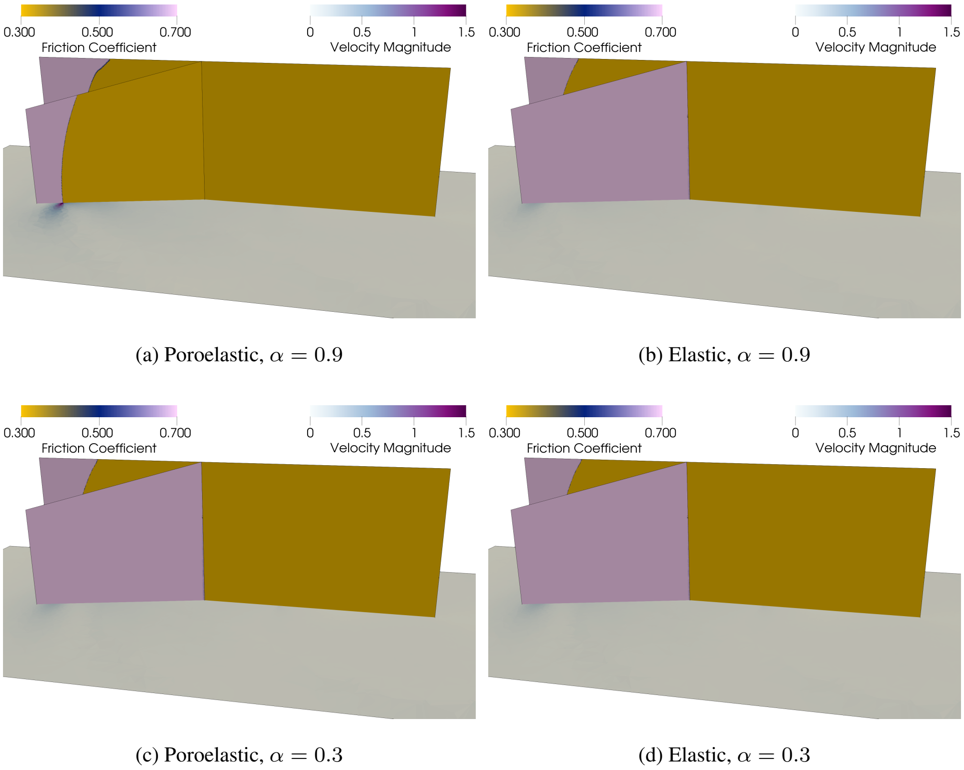

(a) Poroelastic, $\alpha = 0.9$ (b) Elastic, $\alpha = 0.9$

(c) Poroelastic, $\alpha = 0.3$ (d) Elastic, $\alpha = 0.3$

Figure 11. Friction coefficient and wave field in the fault branching scenario after 11 s. Yellow parts of the fault are entirely broken, purple parts are yet intact. The top row shows the results for $\alpha = 0.3$ and the bottom row shows results for $\alpha = 0.9$. On the left, the simulation using the poroelastic material is shown. In the right column, the elastic equivalent is shown. Parts of the branched fault are cropped to visualise the main fault behind it.

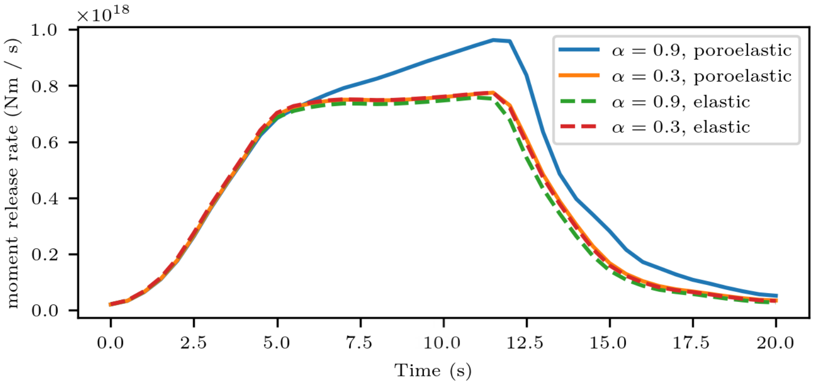

Figure 12. Seismic moment rate release over time for the four possible scenarios ($\alpha = 0.3/\alpha = 0.9$, poroelastic/elastic equivalent) of the branching scenario. For $\alpha = 0.3$, the lines are virtually identical. For $\alpha = 0.9$, we clearly see the additional release of seismic energy caused by the breaking branch after $t = 5$ s.

rheology, the rupture diverted to the branch only, i.e., the main fault remains intact behind the branching point. We thus observe qualitatively different behaviour than for the generic material properties above. This indicates that complex interaction between propagating dynamic rupture and dynamically induced pore-pressure variations determines vastly different dynamic triggering possibilities in a multi-fault system.

3.2.2 *Fault embedded in a poroelastic damage zone*

In the second example application, we analyse dynamic rupture across a fault embedded in a poroelastic fault damage zone. Natural damage zones contain highly fractured rocks (e.g., Chester et al. 1993; Ben-Zion & Sammis 2003) and can impact on rupture dynamic, e.g., inducing pulse-like rupture (Huang & Ampuero 2011; Pelties et al. 2015). In distinction to previous studies, we here approximate a fault zone as a poroelastic material with higher permeability compared to the bedrock. Figure 13 depicts the considered fault zone geometry with the strike-slip fault in the middle and the surrounding damaged zone. We consider the *fault zone* and *basement* materials from (Chang & Segall 2016), which can be found in Table 7. In the fault zone, the S-wave speed is reduced to approximately half of the value of the undamaged material in the basement. We also note that the Biot coefficients increases from 0.2 in the basement to 0.9 in the damaged zone.

We consider the same background stress σ as in the fault branching example (c.f. Equation (5)) and the initial pressure

$$p_0 = \exp\left(-5 \times 10^{-6}\left((x)^2 + (y)^2 + (z+1000)^2\right)\right) \cdot 8.0\,\mathrm{MPa}. \tag{7}$$

Table 6. Realistic material parameters for the poroelastic fault branching dynamic rupture experiment

Parameter	Charcoal granite	Pecos sandstone	Ruhr sandstone	Westerly granite	
K_S	45.0×10^9	39.0×10^9	36.0×10^9	45.0×10^9	Pa
ρ_S	3,000	2,590	2,300	3,000	$\mathrm{kg\,m^{-3}}$
λ_M	22.3×10^9	2.77×10^9	4.33×10^9	15.0×10^9	Pa
μ_M	19.0×10^9	5.90×10^9	13.0×10^9	15.0×10^9	Pa
κ	9.87×10^{-20}	7.90×10^{-16}	1.97×10^{-16}	3.95×10^{-19}	$\mathrm{m^2}$
T	2.0	2.0	2.0	2.0	
ϕ	0.02	0.2	0.02	0.01	
ρ_F	1,000	1,000	1,000	1,000	$\mathrm{kg\,m^{-3}}$
K_F	2.43×10^9	2.30×10^9	2.34×10^9	2.56×10^9	Pa
ν	0.001	0.001	0.001	0.001	Pa s
α	0.222	0.828	0.639	0.444	

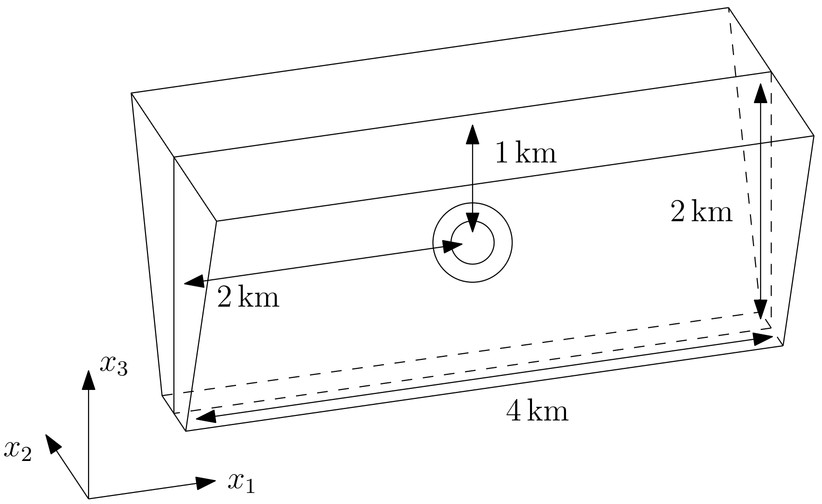

Figure 13. Sketch of the fault geometry together with the surrounding fault zone for the poroelastic fault zone dynamic rupture experiment. The two circles on the fault represent the nucleation area. The top of the fault aligns with the free surface boundary. At the top, the fault zone is $1{,}000\,\mathrm{m}$ wide and at the bottom its width is reduced to $200\,\mathrm{m}$.

The fault is governed by linear slip weakening friction with $\mu_s = 0.7, \mu_d = 0.3, D_c = 0.1\,\mathrm{m}$. In this case, we do not consider shallow frictional on-fault cohesion. The domain of interest is the cuboid $[-12\,\mathrm{km}, 12\,\mathrm{km}] \times [-10\,\mathrm{km}, 10\,\mathrm{km}] \times [-12\,\mathrm{km}, 0\,\mathrm{km}]$. We explicitly mesh the fault and the boundaries of the fault zone. The characteristic edge length is set to $25\,\mathrm{m}$ within the fault zone. with mesh coarsening towards the boundary outside the fault zone. The 3D mesh consists of 2,420,000 tetrahedrons.

Table 7. Material parameters for the poroelastic fault zone dynamic rupture scenario.

Parameter	Basement	Fault zone	
K_S	41.7×10^{9}	80.0×10^{9}	Pa
ρ_S	2.74×10^{3}	2.50×10^{3}	$\mathrm{kg\,m^{-3}}$
λ_M	16.7×10^{9}	4.00×10^{9}	Pa
μ_M	25.0×10^{9}	6.00×10^{9}	Pa
ϕ	0.05	0.02	
κ	2.00×10^{-17}	1.00×10^{-13}	$\mathrm{m^2}$
T	2.0	2.0	
K_F	2.50×10^{9}	2.50×10^{9}	Pa
ρ_F	1.00×10^{3}	1.00×10^{3}	$\mathrm{kg\,m^{-3}}$
ν	1.00×10^{-3}	1.00×10^{-3}	Pa s
α	0.2	0.9	

We run the simulation for 5 s. We compare the results for the poroelastic material with those for the elastic equivalent material, just as we did in the fault branching experiment earlier. Figure 14 compares the slip rate snapshots at the time 1.3 s. We observe almost identical rupture dynamics near the rupture fronts. However, further behind the rupture fronts, the solutions look very differently. The rupture propagates in a pulse-like regime (e.g., Heaton 1990; Gabriel et al. 2012) in the poroelastic material, whereas in a crack-like mode in the elastic equivalent material. We conjecture that the healing in the poroelastic material occurs as a consequence of reduced pore pressure at the fault due to reflected waves from the interface of the poroelastic damage zone.

4 DISCUSSION

Our models illustrate how the poroelastic material model affects seismic wave propagation and rupture dynamics in 3D earthquake scenarios. In high-resolution seismic wave propagation simulations, we find an apparent pressure discontinuity across material interfaces, which increases the requirements on the numerical resolution. While it is known that poroelastic models require increased accuracy at material interfaces, (e.g. Zhang et al. 2022), the apparent pressure discontinuity has not yet been discussed. Nonetheless, we find this pronounced discontinuity in two independent numerical solutions - using SeisSol, a 3D discontinuous Galerkin implementation, and using a 2D finite-difference code. Therefore, we consider this effect to be a key component of the solution of the poroelastic wave equation.

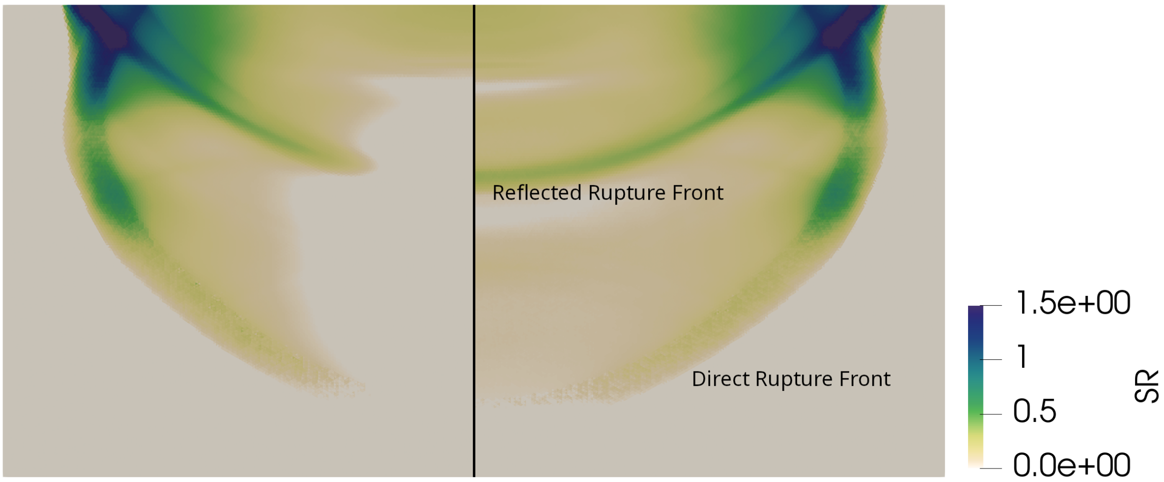

Figure 14. Slip rate magnitude $||\vec{s}||$ on the fault at time $t = 1.3\,\mathrm{s}$ in the fault zone example. *Left*: The results for the poroelastic material. *Right*: The results for the elastic equivalent material. The upper rupture front is the one reflected from the free surface, the lower one propagates directly from the hypocentre. We clearly observe that the rupture arrests earlier in the poroelastic case, compared to the elastic equivalent.

In the case of the Sleipner reservoir scenario, we observe that the Gassmann equivalent serves as a suitable approximation to the poroelastic material describing the displacements of the matrix. However, the fluid pressure is not part of this equivalent elastic model, as it only considers the combined stress, i.e. the stress sustained jointly by the matrix and the fluid. Consequently, how much of the total stress is sustained by the matrix and how much is sustained by the fluid is not captured by the Gassmann approximation.

In our dynamic rupture simulations, we observe that the pressure weakening effect, resulting from changes in effective fault strength due to fluid pressure variations, is not negligible. This effect substantially changes the dynamic rupture characteristics, including rupture velocity and fault-to-fault interaction. Therefore, we argue that the Gassmann equivalent should not be used when fluid pressure is expected to play a vital role in the specific application, as it does not adequately capture such dynamic effects.

The analysis of two complex 3D dynamic rupture scenarios highlights that the pore pressure weakening changes the rupture characteristics significantly. In the first scenario, a secondary fault branch is dynamically activated additionally to the main fault due to poroelastic effects and releases more seismic energy. In the second scenario, dynamic rupture arrests more readily in the poroelastic case, illustrating the influence of fluid pressure on earthquake size.

Further studies are required to investigate the influence of additional material parameters beyond the Biot coefficient α, which may further influence rupture dynamics (Vyas et al. 2023) and seismic wave propagation. Also, analysis of poroelastic effects in more realistic models going beyond idealized benchmark scenarios is beyond the scope of this study.

Our model is limited to the low-frequency regime. We only consider frequencies up to the frequency above which flow through the pores would become turbulent. At frequencies of interest for most seismic applications, the flow in pores can be considered laminar, and thus the low-frequency regime suffices. An example of cases when this assumption is no longer valid are earthquake ground motions simulations in loose water saturated sediments (e.g. Gregor et al. 2021).

This study focuses on rupture dynamics governed by linear slip-weakening friction. Our findings indicate that the dynamic interactions between rupture and dynamically induced pore pressure variations are complex and highly non-linear. Different effects maybe expected for different friction laws and can be the focus of future work. For example, a combination with the more complex concept of rate-and-state friction can easily be integrated in our implementation of dynamic rupture in a poroelastic rheology.

5 CONCLUSIONS

We have successfully incorporated double-couple point sources in poroelastic media using the ADER-DG method within the earthquake simulation software SeisSol. We verified our implementation in canonical models using independent methods, confirming the accuracy and reliability of our approach. Furthermore, we demonstrated the potential of our method through a complex 3D example of poroelastic seismic wave propagation at the Sleipner CCS site. Our analysis shows that the Gassmann elastic equivalent model yields almost identical results to the fully poroelastic model when focusing solely on solid particle velocities. However, the elastic equivalent fails to capture the evolution of pore pressure. Thus, results relying on the elastic equivalent model may be misleading in poroelastic dynamic rupture applications where fault(s) are exposed to dynamically induced variations of pore pressure.

By using suitable numerical fluxes, we have combined the dynamic rupture model with poroelastic rheology using the ADER-DG method. This enhancement to the SeisSol solver allowed us to investigate poroelastic effects on 3D dynamic rupture in complex scenarios. While for seismic wave propagation problems we observe relatively limited effects of the poroelastic rheology that cannot be captured by the elastic equivalent model, we observe significant and intricate effects on dynamic rupture behavior in the poroelastic models that cannot be captured in the elastic equivalent models. In a fault branching scenario, we observe that, depending on the Biot coefficient α, fault branching is facilitated or inhibited. In some cases, dynamic rupture diverted to the branch, leaving the main fault unruptured. When the fault is surrounded by a poroelastic fault zone, we observe pulse-like rupture with a healing front induced by reduced pore pressure due to reflected waves from the boundaries of the poroelastic damage zone.

This study is, to the best of our knowledge, the first to combine dynamic rupture modelling with poroelastic media and 3D tetrahedral meshes. This advancement allows considering more complicated fault geometries, such as fault branching, intersections and poroelastic fault zones. The observed differences between results for the poroelastic model and the Gassmann equivalent model suggest that poroelastic effects may play a crucial role in explaining complex and unexpected dynamics rupture patterns. Since the algorithms have been implemented in the open-source solver SeisSol, this study can be a starting point for other researchers to include poroelastic effects in their models.

ACKNOWLEDGMENTS

We thank Eric M. Dunham for helpful discussions on dynamic rupture in poroelastic media. We thank the Leibniz Supercomputing Centre of the Bavarian Academy of Sciences and Humanities for granting compute time in the project pr83no and pn49ha and the Texas Advanced Computing Center for granting compute time in the project EAR22007. SW and MB acknowledge funding by the Competence Network for Scientific High Performance Computing in Bavaria (KONWIHR). SW, AAG and MB acknowledge funding from the European High Performance Computing Joint Undertaking (JU) under grant agreement No 101093038 and from the German Federal Ministry of Education and Research (BMBF), both for the ChEESE-2P cluster of excellence. AAG acknowledges additional support by the European Union's Horizon 2020 Research and Innovation Programme (TEAR, grant number 852992), Horizon Europe (DT-GEO, grant number 101058129, and Geo-INQUIRE, grant number 101058518), the National Aeronautics and Space Administration (80NSSC20K0495), the National Science Foundation (grant numbers EAR-2225286, EAR-2121568, OAC-2139536, OAC-2311208) and the Southern California Earthquake Center (SCEC awards 22135, 23121).

DATA AVAILABILITY

The simulation results can be reproduced with SeisSol version v1.1.3 (`https://doi.org/10.5281/zenodo.10594058`) using the input data available from zenodo (`https://zenodo.org/records/11401733`).

APPENDIX A: FLUX AND SOURCE MATRICES FOR THE POROELASTIC WAVE EQUATION

Here, we summarise the isotropic version of the matrices A, B, C and E from Equation (1) as they are given by de la Puente (2008). SeisSol and the ADER-DG discretisation expect the governing equations to be expressed in such a first-order formulation. The basic material parameters are the solid density ρ_S and the bulk modulus K_S. Furthermore, the Lamé parameters λ_M, μ_M of the matrix together with porosity ϕ, permeability κ and tortuosity T. The fluid is described by the bulk modulus K_F, the density ρ_F and the viscosity ν. Biot coefficient is defined as $1 - \frac{K_M}{K_S}$ and the coupling modulus is defined as

$$M = \frac{K_S}{1 - \phi - K_M/K_S + \phi K_S/K_F}, \tag{A.1}$$

where the matrix bulk modulus is given by $K_M = \lambda_M + \frac{2}{3}\mu_M$. The flux and source matrices now read:

$$A = \begin{pmatrix}
0 & 0 & 0 & 0 & 0 & 0 & \lambda_M + 2\mu_M + M\alpha^2 & 0 & 0 & 0 & M\alpha & 0 & 0 \\
0 & 0 & 0 & 0 & 0 & 0 & \lambda_M + M\alpha^2 & 0 & 0 & 0 & M\alpha & 0 & 0 \\
0 & 0 & 0 & 0 & 0 & 0 & \lambda_M + M\alpha^2 & 0 & 0 & 0 & M\alpha & 0 & 0 \\
0 & 0 & 0 & 0 & 0 & 0 & 0 & \mu_M & 0 & 0 & 0 & 0 & 0 \\
0 & 0 & 0 & 0 & 0 & 0 & 0 & 0 & 0 & 0 & 0 & 0 & 0 \\
0 & 0 & 0 & 0 & 0 & 0 & 0 & 0 & \mu_M & 0 & 0 & 0 & 0 \\
\frac{1}{\rho^1} & 0 & 0 & 0 & 0 & 0 & 0 & 0 & 0 & \frac{\beta^1}{\rho^1} & 0 & 0 & 0 \\
0 & 0 & 0 & \frac{1}{\rho^1} & 0 & 0 & 0 & 0 & 0 & 0 & 0 & 0 & 0 \\
0 & 0 & 0 & 0 & 0 & \frac{1}{\rho^1} & 0 & 0 & 0 & 0 & 0 & 0 & 0 \\
0 & 0 & 0 & 0 & 0 & 0 & -M\alpha & 0 & 0 & 0 & -M & 0 & 0 \\
\frac{1}{\rho^2} & 0 & 0 & 0 & 0 & 0 & 0 & 0 & 0 & \frac{\beta^2}{\rho^2} & 0 & 0 & 0 \\
0 & 0 & 0 & \frac{1}{\rho^2} & 0 & 0 & 0 & 0 & 0 & 0 & 0 & 0 & 0 \\
0 & 0 & 0 & 0 & 0 & \frac{1}{\rho^2} & 0 & 0 & 0 & 0 & 0 & 0 & 0
\end{pmatrix}, \tag{A.2}$$

$$B = \begin{pmatrix}
0 & 0 & 0 & 0 & 0 & 0 & 0 & \lambda_M + M\alpha^2 & 0 & 0 & 0 & M\alpha & 0 \\
0 & 0 & 0 & 0 & 0 & 0 & 0 & \lambda_M + 2\mu_M + M\alpha^2 & 0 & 0 & 0 & M\alpha & 0 \\
0 & 0 & 0 & 0 & 0 & 0 & 0 & \lambda_M + M\alpha^2 & 0 & 0 & 0 & M\alpha & 0 \\
0 & 0 & 0 & 0 & 0 & 0 & \mu_M & 0 & 0 & 0 & 0 & 0 & 0 \\
0 & 0 & 0 & 0 & 0 & 0 & 0 & 0 & \mu_M & 0 & 0 & 0 & 0 \\
0 & 0 & 0 & 0 & 0 & 0 & 0 & 0 & 0 & 0 & 0 & 0 & 0 \\
0 & 0 & 0 & \frac{1}{\rho^1} & 0 & 0 & 0 & 0 & 0 & 0 & 0 & 0 & 0 \\
0 & \frac{1}{\rho^1} & 0 & 0 & 0 & 0 & 0 & 0 & 0 & \frac{\beta^1}{\rho^1} & 0 & 0 & 0 \\
0 & 0 & 0 & 0 & \frac{1}{\rho^1} & 0 & 0 & 0 & 0 & 0 & 0 & 0 & 0 \\
0 & 0 & 0 & 0 & 0 & 0 & 0 & -M\alpha & 0 & 0 & 0 & -M & 0 \\
0 & 0 & 0 & \frac{1}{\rho^2} & 0 & 0 & 0 & 0 & 0 & 0 & 0 & 0 & 0 \\
0 & \frac{1}{\rho^2} & 0 & 0 & 0 & 0 & 0 & 0 & 0 & \frac{\beta^2}{\rho^2} & 0 & 0 & 0 \\
0 & 0 & 0 & 0 & \frac{1}{\rho^2} & 0 & 0 & 0 & 0 & 0 & 0 & 0 & 0
\end{pmatrix}, \qquad \text{(A.3)}$$

$$C = \begin{pmatrix}
0 & 0 & 0 & 0 & 0 & 0 & 0 & 0 & \lambda_M + M\alpha^2 & 0 & 0 & 0 & M\alpha \\
0 & 0 & 0 & 0 & 0 & 0 & 0 & 0 & \lambda_M + M\alpha^2 & 0 & 0 & 0 & M\alpha \\
0 & 0 & 0 & 0 & 0 & 0 & 0 & 0 & \lambda_M + 2\mu_M + M\alpha^2 & 0 & 0 & 0 & M\alpha \\
0 & 0 & 0 & 0 & 0 & 0 & 0 & 0 & 0 & 0 & 0 & 0 & 0 \\
0 & 0 & 0 & 0 & 0 & 0 & 0 & \mu_M & 0 & 0 & 0 & 0 & 0 \\
0 & 0 & 0 & 0 & 0 & 0 & \mu_M & 0 & 0 & 0 & 0 & 0 & 0 \\
0 & 0 & 0 & 0 & 0 & \frac{1}{\rho^1} & 0 & 0 & 0 & 0 & 0 & 0 & 0 \\
0 & 0 & 0 & 0 & \frac{1}{\rho^1} & 0 & 0 & 0 & 0 & 0 & 0 & 0 & 0 \\
0 & 0 & \frac{1}{\rho^1} & 0 & 0 & 0 & 0 & 0 & 0 & \frac{\beta^1}{\rho^1} & 0 & 0 & 0 \\
0 & 0 & 0 & 0 & 0 & 0 & 0 & 0 & -M\alpha & 0 & 0 & 0 & -M \\
0 & 0 & 0 & 0 & 0 & \frac{1}{\rho^2} & 0 & 0 & 0 & 0 & 0 & 0 & 0 \\
0 & 0 & 0 & 0 & \frac{1}{\rho^2} & 0 & 0 & 0 & 0 & 0 & 0 & 0 & 0 \\
0 & 0 & \frac{1}{\rho^2} & 0 & 0 & 0 & 0 & 0 & 0 & \frac{\beta^2}{\rho^2} & 0 & 0 & 0
\end{pmatrix} \qquad \text{(A.4)}$$

and

$$E = \begin{pmatrix} 0 & 0 & 0 & 0 & 0 & 0 & 0 & 0 & 0 & 0 & 0 & 0 & 0 \\ 0 & 0 & 0 & 0 & 0 & 0 & 0 & 0 & 0 & 0 & 0 & 0 & 0 \\ 0 & 0 & 0 & 0 & 0 & 0 & 0 & 0 & 0 & 0 & 0 & 0 & 0 \\ 0 & 0 & 0 & 0 & 0 & 0 & 0 & 0 & 0 & 0 & 0 & 0 & 0 \\ 0 & 0 & 0 & 0 & 0 & 0 & 0 & 0 & 0 & 0 & 0 & 0 & 0 \\ 0 & 0 & 0 & 0 & 0 & 0 & 0 & 0 & 0 & 0 & 0 & 0 & 0 \\ 0 & 0 & 0 & 0 & 0 & 0 & 0 & 0 & 0 & 0 & \frac{\beta^1\nu}{\rho^1\kappa} & 0 & 0 \\ 0 & 0 & 0 & 0 & 0 & 0 & 0 & 0 & 0 & 0 & 0 & \frac{\beta^1\nu}{\rho^1\kappa} & 0 \\ 0 & 0 & 0 & 0 & 0 & 0 & 0 & 0 & 0 & 0 & 0 & 0 & \frac{\beta^1\nu}{\rho^1\kappa} \\ 0 & 0 & 0 & 0 & 0 & 0 & 0 & 0 & 0 & 0 & 0 & 0 & 0 \\ 0 & 0 & 0 & 0 & 0 & 0 & 0 & 0 & 0 & 0 & \frac{\beta^2\nu}{\rho^2\kappa} & 0 & 0 \\ 0 & 0 & 0 & 0 & 0 & 0 & 0 & 0 & 0 & 0 & 0 & \frac{\beta^2\nu}{\rho^2\kappa} & 0 \\ 0 & 0 & 0 & 0 & 0 & 0 & 0 & 0 & 0 & 0 & 0 & 0 & \frac{\beta^2\nu}{\rho^2\kappa} \end{pmatrix}. \tag{A.5}$$

Here, we have added the auxiliary variables

$$\begin{aligned} \rho &= \phi\rho_F + (1-\phi)\rho_S, \\ m &= \rho_F T/\phi, \\ \rho^1 &= \rho - \rho_F^2/m, \\ \rho^2 &= \rho_F - m\rho/\rho_F, \\ \beta^1 &= \rho_f/m, \\ \beta^2 &= \rho/\rho_F. \end{aligned} \tag{A.6}$$

APPENDIX B: DETAILS OF THE POROELASTIC DYNAMIC RUPTURE SOLVER

We follow the ideas of de la Puente et al. (2009); Duru et al. (2021); Uphoff (2020), who studied dynamic rupture in ADER-DG schemes, to derive the equations for dynamic rupture sources in poroelastic media. An even more detailed derivation can be found in (Wolf 2024).

The first task is to compute the state Q^* at the interface, based on the solution of a Riemann problem. In the poroelastic case, we observe three wave types (P-wave, S-Wave slow P-wave). Therefore, we observe a solution structure as in Figure A1. The states Q^a, Q^b, Q^c, Q^d, Q^e and Q^f can be computed from the Rankine-Hugoniot relations, if we assume continuity of the normal stress, the fluid pressure, the solid velocities and the relative fluid velocity in normal direction at $x = 0$. The states at

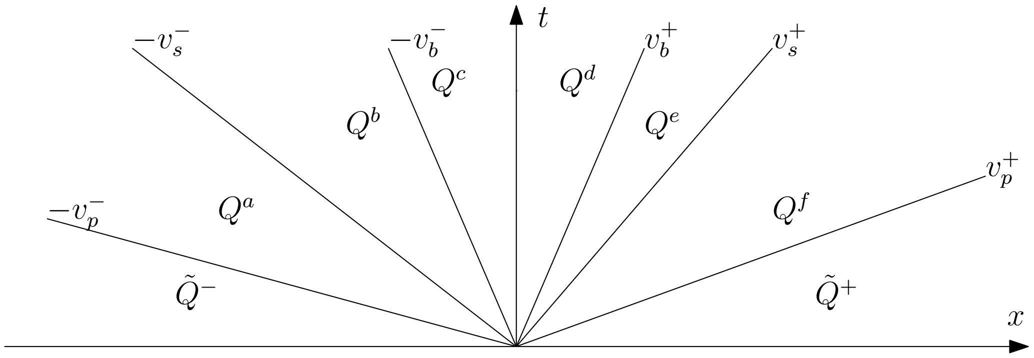

Figure A1. Solution structure of the poroelastic Riemann problem. In addition to the P and S waves, we also observe the slow P wave (subscript b for Biot). We observe left and right-hand states ($\tilde{Q}^-, \tilde{Q}^+$) and six intermediate states $Q^a, Q^b, Q^c, Q^d, Q^e, Q^f$, separated by the slow and fast P and the S waves.

the interface are expressed as

$$\begin{aligned} Q^c - \tilde{Q}^- &= \alpha_1 r_1^- + \alpha_2 r_2^- + \alpha_3 r_3^- + \alpha_4 r_4^- \\ \tilde{Q}^+ - Q^d &= \alpha_{10} r_{10}^+ + \alpha_{11} r_{11}^+ + \alpha_{12} r_{12}^+ + \alpha_{13} r_{13}^+, \end{aligned} \tag{B.1}$$

where α are coefficients and r are eigenvectors of the flux matrix A. The eigenvectors r_5, r_6, r_7, r_8 and r_9 do not contribute to the solution of the Riemann problem, since their respective eigenvalues are all 0. We write down the eigenvectors in a 13×13 matrix and slice out four 4×4 matrices:

$$R = \begin{array}{c|ccccccccccccc|}
 & 1 & 2 & 3 & 4 & 5 & 6 & 7 & 8 & 9 & 10 & 11 & 12 & 13 \\
\sigma_{11} & * & & & * & & & & & & * & & & * \\
\sigma_{22} & * & & & * & * & & & & & * & & & * \\
\sigma_{33} & * & & & * & & * & & & & * & & & * \\
\sigma_{13} & & * & & & & & & & & & & * & \\
\sigma_{23} & & & & & & & * & & & & & & \\
\sigma_{13} & & & * & & & & & & & & * & & \\
u & * & & & * & & & & & & * & & & * \\
v & & * & & & & & & & & & & * & \\
w & & & * & & & & & & & & * & & \\
p & * & & & * & & & & & & * & & & * \\
u_f & * & & & * & & & & & & * & & & * \\
v_f & & * & & & & & & * & & & & * & \\
w_f & & & * & & & & & & * & & * & &
\end{array} . \tag{B.2}$$

Here a $*$ denotes a non-zero entry. The matrices $R_{\mathcal{T}}^-$ and $R_{\mathcal{T}}^+$ correspond to the traction values $\mathcal{T} = \begin{pmatrix}\sigma_{11} & \sigma_{12} & \sigma_{13} & p\end{pmatrix}^T$, whereas the matrices $R_{\mathcal{V}}^-$ and $R_{\mathcal{V}}^+$ correspond to the velocity values $\mathcal{V} = \begin{pmatrix} u & v & w & u_f \end{pmatrix}^T$. In addition, we define $\alpha^- = \begin{pmatrix} \alpha_1 & \alpha_2 & \alpha_3 & \alpha_4 \end{pmatrix}^T$ and $\alpha^+ = \begin{pmatrix} \alpha_{10} & \alpha_{11} & \alpha_{12} & \alpha_{13} \end{pmatrix}^T$. Now, we can write Equation (B.1) as:

$$\begin{aligned} \mathcal{T}^c - \tilde{\mathcal{T}}^- &= R^-_{\mathcal{T}}\alpha^-, \qquad & \mathcal{V}^c - \tilde{\mathcal{V}}^- &= R^-_{\mathcal{V}}\alpha^-, \\ \tilde{\mathcal{T}}^+ - \mathcal{T}^d &= R^+_{\mathcal{T}}\alpha^+, \qquad & \tilde{\mathcal{V}}^+ - \mathcal{V}^d &= R^+_{\mathcal{V}}\alpha^+. \end{aligned} \tag{B.3}$$

At a dynamic boundary interface, the traction parts are continuous: $\mathcal{T}^* = \mathcal{T}^c = \mathcal{T}^d$, but the tangential velocities can be discontinuous. Fault opening is not allowed in our model, thus $u^* = u^c_1 = u^d$ and $u^*_f = u^c_f = u^d_f$. Based on the jump conditions, we can establish a relation that the traction at the interface and the slip rate have to fulfil. Uphoff (2020, eq. 4.50) has derived the formula for the elastic case. If we follow the same steps for the poroelastic case, we find:

$$\begin{aligned} [\![\mathcal{V}^*]\!] &= \mathcal{V}^d - \mathcal{V}^c \\ &= \left(\tilde{\mathcal{V}}^+ - R^+_{\mathcal{V}}\alpha^+\right) - \left(\tilde{\mathcal{V}}^- + R^-_{\mathcal{V}}\alpha^-\right) \\ &= \tilde{\mathcal{V}}^+ - \tilde{\mathcal{V}}^- - R^+_{\mathcal{V}}\left(R^+_{\mathcal{T}}\right)^{-1}\left(\tilde{\mathcal{T}}^+ - \mathcal{T}^d\right) - R^-_{\mathcal{V}}\left(R^-_{\mathcal{T}}\right)^{-1}\left(\mathcal{T}^c - \tilde{\mathcal{T}}^-\right) \\ &= \tilde{\mathcal{V}}^+ - \tilde{\mathcal{V}}^- - R^+_{\mathcal{V}}\left(R^+_{\mathcal{T}}\right)^{-1}\tilde{\mathcal{T}}^+ + R^-_{\mathcal{V}}\left(R^-_{\mathcal{T}}\right)^{-1}\tilde{\mathcal{T}}^- \\ &+ \left(R^+_{\mathcal{V}}\left(R^+_{\mathcal{T}}\right)^{-1} - R^-_{\mathcal{V}}\left(R^-_{\mathcal{T}}\right)^{-1}\right)\mathcal{T}^*. \end{aligned} \tag{B.4}$$

We define the matrices $(Z^\pm)^{-1} := R^\pm_{\mathcal{V}}\left(R^\pm_{\mathcal{T}}\right)^{-1}$ and $\eta^{-1} := R^-_{\mathcal{V}}\left(R^-_{\mathcal{T}}\right)^{-1} - R^+_{\mathcal{V}}\left(R^+_{\mathcal{T}}\right)^{-1}$. In analogy to eq. 4.50 in Uphoff (2020), we write:

$$[\![\mathcal{V}^*]\!] = \left[\!\!\left[\tilde{\mathcal{V}}\right]\!\!\right] - \left(Z^+\right)^{-1}\tilde{\mathcal{T}}^+ + \left(Z^-\right)^{-1}\tilde{\mathcal{T}}^- + \eta^{-1}\mathcal{T}^*. \tag{B.5}$$

The structure of the involved matrix only couples u and u_f, but the tangential velocity components v and w are still independent as in the elastic case. Similar to the elastic case, we define

$$\Theta := \eta\left(\left[\!\!\left[\tilde{\mathcal{V}}\right]\!\!\right] - \left(Z^+\right)^{-1}\tilde{\mathcal{T}}^+ + \left(Z^-\right)^{-1}\tilde{\mathcal{T}}^-\right). \tag{B.6}$$

This allows us to relate the tractions and velocities at the fault:

$$\eta[\![\mathcal{V}^*]\!] + \mathcal{T}^* = \Theta. \tag{B.7}$$

Now, the task is to find velocities and tractions $\mathcal{V}^{\mathrm{DR}}$ and $\mathcal{T}^{\mathrm{DR}}$, which are consistent with the friction law and Equation (B.7). We already have established continuity of u and u_f, thus $[\![u^{\mathrm{DR}}]\!] = 0$ and $\left[\!\!\left[u_f^{\mathrm{DR}}\right]\!\!\right] = 0$. As a direct consequence, we obtain $\sigma^{\mathrm{DR}}_{11} = \Theta_1$ and $p^{\mathrm{DR}} = \Theta_4$. For the tangential parts of the traction, we have to solve a system of linear equations:

$$\begin{aligned} \tau\left[\!\left[\mathcal{V}^{\mathrm{DR}}_2\right]\!\right] &= \mathcal{T}^{\mathrm{DR}}_2\|s\|, \quad & \eta_{22}\left[\!\left[\mathcal{V}^{\mathrm{DR}}_2\right]\!\right] + \mathcal{T}^{\mathrm{DR}}_2 &= \Theta_2, \\ \tau\left[\!\left[\mathcal{V}^{\mathrm{DR}}_3\right]\!\right] &= \mathcal{T}^{\mathrm{DR}}_3\|s\|, \quad & \eta_{33}\left[\!\left[\mathcal{V}^{\mathrm{DR}}_3\right]\!\right] + \mathcal{T}^{\mathrm{DR}}_3 &= \Theta_3, \end{aligned} \tag{B.8}$$

where η_{22} and η_{33} are coefficients of the matrix η. The fault strength $\tau(\|\vec{s}\|, \phi) = \mu_f(\|\vec{s}\|, \psi) \cdot \sigma_n$ depends on the friction parameter μ_f and the effective normal stress σ_n. Depending on the choice of friction law, the friction parameter depends on the slip rate $\|\vec{s}\|$ and the state variable ϕ. In the isotropic poroelastic case, the values η_{22} and η_{33} coincide. We define $\eta := \eta_{22} = \eta_{33}$. In the isotropic poroelastic case, the values η_{22} and η_{33} coincide. We recall that $\|\vec{s}\| = \sqrt{[\![\mathcal{V}_2^{\mathrm{DR}}]\!]^2 + [\![\mathcal{V}_3^{\mathrm{DR}}]\!]^2}$ and obtain the equation

$$\tau_S(\|\vec{s}\|, \phi) + \eta\|\vec{s}\| = \sqrt{\Theta_2^2 + \Theta_3^2}, \tag{B.9}$$

which has to be solved for the slip rate $\|\vec{s}\|$.

We recall that the fluid pressure has a weakening effect on the fault: When computing the fault strength $\tau = \max\left(0, -\mu_f\tilde{\sigma_n} - C\right)$, we have to consider the augmented normal stress $\tilde{\sigma}_n = \mathcal{T}_1 - p$. We use a Newton-Raphson solver to calculate the slip rate based on Equation (B.9). Once the slip rate $\|\vec{s}\|$ is known, we compute its two components and the two tractions from Equation (B.8). Now, the imposed state $\mathcal{T}^{\mathrm{DR}}$ and the slip rates $[\![\mathcal{V}^{\mathrm{DR}}]\!]$ are known. We use Equation (B.4) to compute $\mathcal{V}^c$ and $\mathcal{V}^d$ from From Equation (B.1), we conclude that we can compute $\mathcal{V}^c$ and $\mathcal{V}^d$ from $\mathcal{V}^-$, $\mathcal{V}^+$ and $\alpha^\pm$. The coefficients $\alpha^\pm$ solely depend on the traction values $\mathcal{T}^c$, $\mathcal{T}^d$, $\mathcal{T}^-$ and $\mathcal{T}^+$, which are known at this time already. We conclude

$$\begin{aligned}
\mathcal{V}^c &= \mathcal{V}^- + R_{\mathcal{V}}^-\alpha^- \\
&= \mathcal{V}^- + R_{\mathcal{V}}^-\left(R_{\mathcal{T}}^-\right)^{-1}\left(\mathcal{T}^c - \mathcal{T}^-\right) \\
&= \mathcal{V}^- + \left(Z^-\right)^{-1}\left(\widehat{\mathcal{T}} - \mathcal{T}^-\right) \\
\mathcal{V}^d &= \mathcal{V}^+ - R_{\mathcal{V}}^+\alpha^+ \\
&= \mathcal{V}^+ - R_{\mathcal{V}}^+\left(R_{\mathcal{T}}^+\right)^{-1}\left(\mathcal{T}^+ - \mathcal{T}^d\right) \\
&= \mathcal{V}^+ - \left(Z^+\right)^{-1}\left(\mathcal{T}^+ - \widehat{\mathcal{T}}\right).
\end{aligned} \tag{B.10}$$

With this equation, the states $\mathcal{Q}^c$ and $\mathcal{Q}^d$ are known. They are consistent with the Rankine-Hugoniot jump conditions as well as with the friction law. These states can now be used as imposed states at the interface to compute the upwind flux.

APPENDIX C: MISFIT TABLES FOR THE HOMOGENEOUS FULL-SPACE TEST CASE

Table A1. Misfits at all receiver positions for the homogeneous full space, when the pores are filled with an inviscid fluid (all values in %).

Receiver	EM u	PM u	EM w	PM w	EM u_f	PM u_f	EM w_f	PM w_f
1	0.05	0.0	0.71	0.11	0.47	0.0	0.84	0.11
2	0.06	0.0	0.71	0.10	0.58	0.0	0.78	0.11
3	1.12	0.11	0.82	0.11	0.81	0.14	0.81	0.16
4	1.15	0.12	0.96	0.11	1.52	0.41	1.60	0.45
5	0.35	0.06	0.70	0.14	1.20	0.12	0.88	0.11
6	0.34	0.06	0.69	0.14	1.10	0.20	0.86	0.17
7	0.08	0.0	0.68	0.10	0.43	0.0	0.71	0.10
8	0.06	0.0	0.65	0.10	0.58	0.0	0.66	0.10
9	1.28	0.21	1.22	0.22	4.22	1.31	4.71	1.43
10	1.52	0.35	1.47	0.36	7.86	2.47	7.91	2.45
11	0.34	0.07	0.65	0.14	4.56	1.43	2.12	0.66
12	0.36	0.09	0.63	0.14	6.83	2.19	2.76	0.87

Table A2. Misfits at all receivers for the homogeneous full space scenario, when the pores are filled with a viscous fluid (all values in %).

Receiver	EM u	PM u	EM w	PM w	EM u_f	PM u_f	EM w_f	PM w_f
1	0.05	0.0	0.72	0.10	0.08	0.0	0.82	0.12
2	0.06	0.0	0.71	0.10	0.09	0.0	0.81	0.12
3	1.16	0.11	0.84	0.10	1.71	0.15	1.31	0.12
4	1.19	0.11	1.05	0.09	1.80	0.14	1.78	0.12
5	0.34	0.06	0.70	0.13	0.34	0.07	0.78	0.16
6	0.33	0.06	0.69	0.14	0.36	0.06	0.76	0.15
7	0.08	0.0	0.68	0.10	0.14	0.0	0.77	0.12
8	0.07	0.0	0.66	0.10	0.11	0.0	0.76	0.13
9	1.16	0.10	1.04	0.10	1.76	0.14	1.63	0.13
10	1.13	0.10	1.01	0.10	1.80	0.13	1.51	0.14
11	0.31	0.06	0.65	0.14	1.87	0.15	1.60	0.22
12	0.30	0.06	0.63	0.14	0.46	0.05	0.77	0.15

REFERENCES

Aagaard, B. T., Knepley, M. G., & Williams, C. A., 2013. A domain decomposition approach to implementing fault slip in finite-element models of quasi-static and dynamic crustal deformation, *Journal of Geophysical Research: Solid Earth*, **118**(6), 3059–3079.

Aki, K. & Richards, P., 2002. *Quantitative Seismology, 2nd Edition*, University Science Books, U.S., Sausalito, California, 2nd edn.

Andrews, D. J., 1976. Rupture velocity of plane strain shear cracks, *Journal of Geophysical Research*, **81**(32), 5679–5687.

Barall, M., 2009. A grid-doubling finite-element technique for calculating dynamic three-dimensional spontaneous rupture on an earthquake fault, *Geophysical Journal International*, **178**(2), 845–859.

Ben-Zion, Y. & Sammis, C. G., 2003. Characterization of Fault Zones, *Pure and Applied Geophysics*, **160**(3), 677–715.

Berryman, J. G., 1980. Confirmation of Biot's theory, *Applied Physics Letters*, **37**(4), 382–384.

Biot, M. A., 1956a. Theory of Propagation of Elastic Waves in a Fluid-Saturated Porous Solid. I. Low-Frequency Range, *The Journal of the Acoustical Society of America*, **28**(2), 168–178.

Biot, M. A., 1956b. Theory of Propagation of Elastic Waves in a Fluid-Saturated Porous Solid. II. Higher Frequency Range, *The Journal of the Acoustical Society of America*, **28**(2), 179–191.

Biot, M. A., 1956c. Theory of Deformation of a Porous Viscoelastic Anisotropic Solid, *Journal of Applied Physics*, **27**(5), 459–467.

Biot, M. A., 1962. Mechanics of Deformation and Acoustic Propagation in Porous Media, *Journal of Applied Physics*, **33**(4), 1482–1498.

Carcione, J. M., 2001. Energy balance and fundamental relations in dynamic anisotropic poro-viscoelasticity, *Proceedings of the Royal Society of London. Series A: Mathematical, Physical and Engineering Sciences*, pp. 331–348.

Carcione, J. M., 2015. *Wave Fields in Real Media*, Elsevier, Oxford, third edition edn.

Carcione, J. M., Morency, C., & Santos, J. E., 2010. Computational poroelasticity — A review, *Geophysics*, pp. 75A229–75A243.

eds Castagna, J. P. & Backus, M. M., 1993. *Offset-Dependent Reflectivity—Theory and Practice of AVO Analysis*, Society of Exploration Geophysicists.

Chang, K. W. & Segall, P., 2016. Injection-induced seismicity on basement faults including poroelastic stressing, *Journal of Geophysical Research: Solid Earth*, **121**(4), 2708–2726.

Chester, F. M., Evans, J. P., & Biegel, R. L., 1993. Internal structure and weakening mechanisms of the san andreas fault, *Journal of Geophysical Research: Solid Earth*, **98**(B1), 771–786.

Cruz-Atienza, V. M. & Virieux, J., 2004. Dynamic rupture simulation of non-planar faults with a finite-difference approach, *Geophysical Journal International*, **158**(3), 939–954.

Day, S. M., 1982. Three-dimensional finite difference simulation of fault dynamics: Rectangular faults with fixed rupture velocity, *Bulletin of the Seismological Society of America*, **72**(3), 705–727.

De Barros, L., Dietrich, M., & Valette, B., 2010. Full waveform inversion of seismic waves reflected in a stratified porous medium: Full waveform inversion in porous medium, *Geophysical Journal International*, **182**(3), 1543–1556.

de la Puente, J., 2008. *Seismic Wave Simulation for Complex Rheologies on Unstructured Meshes*, Ph.D. thesis, Ludwig-Maximilians-Universität München, Munich.

de la Puente, J., Dumbser, M., Käser, M., & Igel, H., 2008. Discontinuous Galerkin methods for wave propagation in poroelastic media, *GEOPHYSICS*, **73**(5), T77–T97.

de la Puente, J., Ampuero, J.-P., & Käser, M., 2009. Dynamic rupture modeling on unstructured meshes using a discontinuous Galerkin method, *Journal of Geophysical Research: Solid Earth*, **114**(B10).

De Simone, S., Darcel, C., Kasani, H. A., Mas Ivars, D., & Davy, P., 2023. Equivalent Biot and Skempton Poroelastic Coefficients for a Fractured Rock Mass from a DFN Approach, *Rock Mechanics and Rock Engineering*, **56**(12).

Detournay, E. & Cheng, A. H. D., 1993. Fundamentals of Poroelasticity, in *Analysis and Design Methods*, pp. 113–171, ed. Fairhurst, C., Pergamon, Oxford.

Duan, B., 2012. Dynamic rupture of the 2011 Mw 9.0 Tohoku-Oki earthquake: Roles of a possible subducting seamount, *Journal of Geophysical Research: Solid Earth*, **117**(B5), 1–16.

Dumbser, M. & Käser, M., 2006. An arbitrary high-order discontinuous Galerkin method for elastic waves on unstructured meshes - II. The three-dimensional isotropic case, *Geophysical Journal International*, **167**(1), 319–336.

Dumbser, M., Balsara, D. S., Toro, E. F., & Munz, C.-D., 2008. A unified framework for the construction of one-step finite volume and discontinuous Galerkin schemes on unstructured meshes, *Journal of Computational Physics*, **227**(18), 8209–8253.

Dunham, E. M. & Rice, J. R., 2008. Earthquake slip between dissimilar poroelastic materials, *Journal of Geophysical Research: Solid Earth*, **113**(B9).

Dupuy, B., Garambois, S., & Virieux, J., 2016. Estimation of rock physics properties from seismic attributes — Part 1: Strategy and sensitivity analysis, *GEOPHYSICS*, **81**(3), M35–M53.

Duru, K. & Dunham, E. M., 2016. Dynamic earthquake rupture simulations on nonplanar faults embedded in 3D geometrically complex, heterogeneous elastic solids, *Journal of Computational Physics*, **305**, 185–207.

Duru, K., Rannabauer, L., Gabriel, A.-A., & Igel, H., 2021. A New Discontinuous Galerkin Method for Elastic Waves with Physically Motivated Numerical Fluxes, *Journal of Scientific Computing*, **88**(3), 1–32.

Dutta, N. C. & Odé, H., 1983. Seismic reflections from a gas-water contact, *GEOPHYSICS*, **48**(2), 148–162, Publisher: Society of Exploration Geophysicists.

Ely, G. P., Day, S. M., & Minster, J.-B., 2009. A support-operator method for 3-D rupture dynamics, *Geophysical Journal International*, **177**(3), 1140–1150.

Ely, G. P., Day, S. M., & Minster, J.-B., 2010. Dynamic Rupture Models for the Southern San Andreas Fault, *Bulletin of the Seismological Society of America*, **100**(1), 131–150.

Equinor, 2019. Sleipner 2019 Benchmark Model, https://co2datashare.org/dataset/sleipner-2019-benchmark-model.

Gabriel, A.-A., 2021. A unified first-order hyperbolic model for nonlinear dynamic rupture processes in diffuse fracture zones, *Philosophical Transactions of the Royal Society A*, **379**(2196), 20200130.

Gabriel, A.-A., Ampuero, J.-P., Dalguer, L. A., & Mai, P. M., 2012. The transition of dynamic rupture styles in elastic media under velocity-weakening friction, *Journal of Geophysical Research: Solid Earth*, **117**.

Gabriel, A.-A., Ulrich, T., Marchandon, M., Biemiller, J., & Rekoske, J., 2023. 3D Dynamic Rupture Modeling of the 6 February 2023, Kahramanmaraş, Turkey Mw 7.8 and 7.7 Earthquake Doublet Using Early Observations, *The Seismic Record*, **3**(4), 342–356.

Gardner, G. H. F., Gardner, L. W., & Gregory, A. R., 1974. Formation velocity and density; the diagnostic basics for stratigraphic traps, *Geophysics*, **39**(6), 770–780.

Gassmann, F., 1951. Über die Elastizität poröser Medien, *Vierteljahrsschrift der naturforschenden Gesellschaft in Zürich*, **96**.

Gassner, G., Dumbser, M., Hindenlang, F., & Munz, C.-D., 2011. Explicit one-step time discretizations for discontinuous Galerkin and finite volume schemes based on local predictors, *Journal of Computational Physics*, **230**(11), 4232–4247.

Gregor, D., Moczo, P., Kristek, J., Mesgouez, A., Lefeuve-Mesgouez, G., & Kristekova, M., 2021. Subcell-resolution finite-difference modelling of seismic waves in Biot and JKD poroelastic media, *Geophysical Journal International*, **224**(2), 760–794.

Gregor, D., Moczo, P., Kristek, J., Mesgouez, A., Lefeuve-Mesgouez, G., Morency, C., Diaz, J., & Kristekova, M., 2022. Seismic waves in medium with poroelastic/elastic interfaces: A two-dimensional P-SV finite-difference modelling, *Geophysical Journal International*, **228**(1), 551–588.

Harris, R. A., Barall, M., Archuleta, R., Dunham, E., Aagaard, B., Ampuero, J. P., Bhat, H., Cruz-Atienza, V., Dalguer, L., Dawson, P., Day, S., Duan, B., Ely, G., Kaneko, Y., Kase, Y., Lapusta, N., Liu, Y., Ma, S., Oglesby, D., Olsen, K., Pitarka, A., Song, S., & Templeton, E., 2009. The SCEC/USGS Dynamic Earthquake Rupture Code Verification Exercise, *Seismological Research Letters*, **80**(1), 119–126.

Harris, R. A., Barall, M., Andrews, D. J., Duan, B., Ma, S., Dunham, E. M., Gabriel, A.-A., Kaneko, Y., Kase, Y., Aagaard, B. T., Oglesby, D. D., Ampuero, J.-P., Hanks, T. C., & Abrahamson, N., 2011. Verifying a Computational Method for Predicting Extreme Ground Motion, *Seismological Research Letters*, **82**(5), 638–644.

Harris, R. A., Barall, M., Aagaard, B., Ma, S., Roten, D., Olsen, K., Duan, B., Liu, D., Luo, B., Bai, K., Ampuero, J., Kaneko, Y., Gabriel, A., Duru, K., Ulrich, T., Wollherr, S., Shi, Z., Dunham, E., Bydlon, S., Zhang, Z., Chen, X., Somala, S. N., Pelties, C., Tago, J., Cruz-Atienza, V. M., Kozdon, J., Daub, E., Aslam, K., Kase, Y., Withers, K., & Dalguer, L., 2018. A Suite of Exercises for Verifying Dynamic Earthquake Rupture Codes, *Seismological Research Letters*, **89**(3), 1146–1162.

Harris, R. A., Barall, M., Lockner, D. A., Moore, D. E., Ponce, D. A., Graymer, R., Funning, G., Morrow, C. A., Kyriakopoulos, C., & Eberhart-Phillips, D., 2021. A geology and geodesy based model of dynamic earthquake rupture on the rodgers creek-hayward-calaveras fault system, california, *Journal of Geophysical*

Research: Solid Earth, **126**(3), e2020JB020577.

Hayek, J. N., May, D. A., Pranger, C., & Gabriel, A.-A., 2023. A diffuse interface method for earthquake rupture dynamics based on a phase-field model, *Journal of Geophysical Research: Solid Earth*, **128**(12), e2023JB027143.

Heaton, T. H., 1990. Evidence for and implications of self-healing pulses of slip in earthquake rupture, *Physics of the Earth and Planetary Interiors*, **64**.

Heimisson, E. R., Rudnicki, J., & Lapusta, N., 2021. Dilatancy and compaction of a rate-and-state fault in a poroelastic medium: Linearized stability analysis, *Journal of Geophysical Research: Solid Earth*, **126**(8), e2021JB022071.

Hesthaven, J. S. & Warburton, T., 2008. *Nodal Discontinuous Galerkin Methods: Algorithms, Analysis, and Applications*, Texts in Applied Mathematics, Springer-Verlag, New York.

Huang, Y. & Ampuero, J.-P., 2011. Pulse-like ruptures induced by low-velocity fault zones, *Journal of Geophysical Research: Solid Earth*, **116**(B12), _eprint: https://onlinelibrary.wiley.com/doi/pdf/10.1029/2011JB008684.

Jha, B. & Juanes, R., 2014. Coupled multiphase flow and poromechanics: A computational model of pore pressure effects on fault slip and earthquake triggering, *Water Resources Research*, **50**(5), 3776–3808.

Kammer, D. S., McLaskey, G. C., Abercrombie, R. E., Ampuero, J.-P., Cattania, C., Cocco, M., Dal Zilio, L., Dresen, G., Gabriel, A.-A., Ke, C.-Y., et al., 2024. Earthquake energy dissipation in a fracture mechanics framework, *Nature Communications*, **15**(1), 4736.

Kaneko, Y., Lapusta, N., & Ampuero, J.-P., 2008. Spectral element modeling of spontaneous earthquake rupture on rate and state faults: Effect of velocity-strengthening friction at shallow depths, *Journal of Geophysical Research: Solid Earth*, **113**(B9), 1–17.

Karpfinger, F., Müller, T. M., & Gurevich, B., 2009. Green's functions and radiation patterns in poroelastic solids revisited, *Geophysical Journal International*, **178**(1), 327–337.

Kristekova, M., Kristek, J., Moczo, P., & Day, S. M., 2006. Misfit Criteria for Quantitative Comparison of Seismograms, *Bulletin of the Seismological Society of America*, **96**(5), 1836–1850.

Kristekova, M., Kristek, J., & Moczo, P., 2009. Time-frequency misfit and goodness-of-fit criteria for quantitative comparison of time signals, *Geophysical Journal International*, **178**(2), 813–825.

Käser, M., Hermann, V., & de la Puente, J., 2008. Quantitative accuracy analysis of the discontinuous Galerkin method for seismic wave propagation, *Geophysical Journal International*, **173**(3), 990–999.

LeVeque, R. J., 2002. *Finite Volume Methods for Hyperbolic Problems*, Cambridge Texts in Applied Mathematics, Cambridge University Press, Cambridge.

Li, Z. & Zhang, H., 2023. Time-domain Green's function in poroelastic mediums and its application to 3-D spontaneous rupture simulation, *Geophysical Journal International*, **234**(3), 2231–2254.

Masson, Y. J., Pride, S. R., & Nihei, K. T., 2006. Finite difference modeling of Biot's poroelastic equations at seismic frequencies, *Journal of Geophysical Research*, **111**(B10), 1–13.

Mavko, G., Mukerji, T., & Dvorkin, J., 2009. *The Rock Physics Handbook: Tools for Seismic Analysis of*

Porous Media, Cambridge University Press, Cambridge, 2nd edn.

Moczo, P., Jozef, K., & Martin, G., 2014. *The Finite-Difference Modelling of Earthquake Motions: Waves and Ruptures*, Cambridge University Press.

Moczo, P., Gregor, D., Kristek, J., & de la Puente, J., 2019. A discrete representation of material heterogeneity for the finite-difference modelling of seismic wave propagation in a poroelastic medium, *Geophysical Journal International*, **216**(2), 1072–1099.

Morency, C., Luo, Y., & Tromp, J., 2011. Acoustic, elastic and poroelastic simulations of CO2 sequestration crosswell monitoring based on spectral-element and adjoint methods: CO2 sequestration monitoring, *Geophysical Journal International*, **185**(2), 955–966.

Oglesby, D. D., Archuleta, R. J., & Nielsen, S. B., 1998. Earthquakes on dipping faults: The effects of broken symmetry, *Science*, **280**(5366), 1055–1059.

Okubo, K., Rougier, E., Lei, Z., & Bhat, H. S., 2020. Modeling earthquakes with off-fault damage using the combined finite-discrete element method, *Computational particle mechanics*, **7**(5), 1057–1072.

Pampillón, P., Santillán, D., Mosquera, J. C., & Cueto-Felgueroso, L., 2018. Dynamic and Quasi-Dynamic Modeling of Injection-Induced Earthquakes in Poroelastic Media, *Journal of Geophysical Research: Solid Earth*, **123**(7), 5730–5759.

Pampillón, P., Santillán, D., Mosquera, J. C., & Cueto-Felgueroso, L., 2023. The role of pore fluids in supershear earthquake ruptures, *Scientific Reports*, **13**(1), 1–10.

Pelties, C., de la Puente, J., Ampuero, J.-P., Brietzke, G. B., & Käser, M., 2012a. Three-dimensional dynamic rupture simulation with a high-order discontinuous Galerkin method on unstructured tetrahedral meshes, *Journal of Geophysical Research: Solid Earth*, **117**(B2).

Pelties, C., de la Puente, J., Ampuero, J.-P., Brietzke, G. B., & Käser, M., 2012b. Three-dimensional dynamic rupture simulation with a high-order discontinuous Galerkin method on unstructured tetrahedral meshes, *Journal of Geophysical Research: Solid Earth*, **117**(B2), 1–15.

Pelties, C., Huang, Y., & Ampuero, J.-P., 2015. Pulse-Like Rupture Induced by Three-Dimensional Fault Zone Flower Structures, *Pure and Applied Geophysics*, **172**(5), 1229–1241.

Plona, T. J., 1980. Observation of a second bulk compressional wave in a porous medium at ultrasonic frequencies, *Applied Physics Letters*, **36**(4), 259–261.

Ramos, M. D., Thakur, P., Huang, Y., Harris, R. A., & Ryan, K. J., 2022. Working with Dynamic Earthquake Rupture Models: A Practical Guide, *Seismological Research Letters*, **93**(4), 2096–2110.

Rudnicki, J. W. & Rice, J. R., 2006. Effective normal stress alteration due to pore pressure changes induced by dynamic slip propagation on a plane between dissimilar materials, *Journal of Geophysical Research: Solid Earth*, **111**(B10).

Sambridge, M., 1999. Geophysical inversion with a neighbourhood algorithm—I. Searching a parameter space, *Geophysical Journal International*, **138**(2), 479–494.

Song, Y. & Rudnicki, J. W., 2017. Plane-strain shear dislocation on a leaky plane in a poroelastic solid, *Journal of Applied Mechanics*, **84**(2), 021008.

Taufiqurrahman, T., Gabriel, A., Ulrich, T., Valentová, L., & Gallovič, F., 2022. Broadband Dynamic Rupture Modeling With Fractal Fault Roughness, Frictional Heterogeneity, Viscoelasticity and Topography: The 2016 $M_{\rm w}$ 6.2 Amatrice, Italy Earthquake, *Geophysical Research Letters*, **49**(22), e2022GL098872.

Traub, B., 2008. 2ReMoVe - WP 3.4: Sleipner AVO study on synthetic Sleipner data, Tech. rep., SINTEF Petroleum Research.

Ulrich, T., Gabriel, A.-A., Ampuero, J.-P., & Xu, W., 2019. Dynamic viability of the 2016 Mw 7.8 Kaikōura earthquake cascade on weak crustal faults, *Nature Communications*, **10**(1), 1–16.

Uphoff, C., 2020. *Flexible Model Extension and Optimisation for Earthquake Simulations at Extreme Scales*, Ph.D. thesis, Technische Universität München.

Uphoff, C., Rettenberger, S., Bader, M., Madden, E. H., Ulrich, T., Wollherr, S., & Gabriel, A.-A., 2017. Extreme Scale Multi-physics Simulations of the Tsunamigenic 2004 Sumatra Megathrust Earthquake, in *Proceedings of the International Conference for High Performance Computing, Networking, Storage and Analysis*, SC '17, pp. 21:1–21:16, ACM, New York, NY, USA.

Vernik, L., Fisher, D., & Bahret, S., 2002. Estimation of net-to-gross from P and S impedance in deepwater turbidites, *The Leading Edge*, **21**(4), 380–387.

Virieux, J. & Madariaga, R., 1982. Dynamic faulting studied by a finite difference method, *Bulletin of the Seismological Society of America*, **72**(2), 345–369.

Vyas, J. C., Gabriel, A.-A., Ulrich, T., Mai, P. M., & Ampuero, J.-P., 2023. How does thermal pressurization of pore fluids affect 3d strike-slip earthquake dynamics and ground motions?, *Bulletin of the Seismological Society of America*, **113**(5), 1992–2008.

Wolf, S., 2024. *High-Performance Earthquake Simulations with Advanced Material Models*, Ph.D. thesis, Technische Universität München.

Wolf, S., Galis, M., Uphoff, C., Gabriel, A.-A., Moczo, P., Gregor, D., & Bader, M., 2022. An efficient ADER-DG local time stepping scheme for 3D HPC simulation of seismic waves in poroelastic media, *Journal of Computational Physics*, **455**, 1–29.

Yan, H., 2017. *Rock Physics Inversion for CO2 Characterization at Sleipner*, Master's thesis, NTNU.

Yang, Z. & Juanes, R., 2018. Two sides of a fault: Grain-scale analysis of pore pressure control on fault slip, *Physical Review E*, **97**(2), 022906.

Zhang, H., Sun, Y.-C., Ren, H., Zhang, W., Huang, Q., & Chen, X., 2022. Discontinuous curvilinear collocated grid combined with nonuniform time step Runge-Kutta scheme for poroelastic finite-difference modeling, *Geophysics*, **88**(1), T1–T12.

Zhang, Z., Zhang, W., & Chen, X., 2014. Three-dimensional curved grid finite-difference modelling for non-planar rupture dynamics, *Geophysical Journal International*, **199**(2), 860–879.

Zhu, X. & McMechan, G. A., 1991. Numerical simulation of seismic responses of poroelastic reservoirs using Biot theory, *GEOPHYSICS*, **56**(3), 328–339.

This paper has been produced using the Blackwell Scientific Publications GJI LaTeX2e class file.